Imaging the (un)imaginable of the Barrier Immune system

Guo, N.

Chapter 4

Mass Cytometric Analysis of Early Stage Mycosis Fungoides

Nannan Guo[1], Li Jia[1], Coby Out-Luiting[2], Noel F. C. C. de Miranda[3], Rein Willemze[2], Frits Koning[1], Maarten Vermeer[2], Koen Quint[2*]

[1]Department of Immunology, Leiden University Medical Center, Leiden, The Netherlands
[2]Department of Dermatology, Leiden University Medical Center, Leiden, The Netherlands
[3]Department of Pathology, Leiden University Medical Center, Leiden, The Netherlands

[*]**Correspondence**

Cells 2022, 11, 1062.

Abstract

Mycosis Fungoides (MF) is the most common subtype of cutaneous T-cell lymphoma. Early stage disease is characterized by superficial infiltrates of small to medium-sized atypical epidermotropic T-lymphocytes that are clonal related. Nevertheless, the percentage of atypical T cells is low with many admixed reactive immune cells. Despite earlier studies the composition and spatial characteristics of the cutaneous lymphocytic infiltrate has been incompletely characterized. Here, we applied mass cytometry to profile the immune system in skin biopsies of patients with early stage MF and in normal skin from healthy individuals. Single cell suspensions were prepared and labelled with a 43-antibody panel and data were acquired on a Helios mass cytometer. Unbiased hierarchical clustering of the data identified the major immune lineages and heterogeneity therein. This revealed patient-unique cell clusters in both the $CD4^+$ and myeloid cell compartment but also phenotypically distinct cell clusters that were shared by most patients. To characterize the immune compartment in the tissue context, we developed a 36-antibody panel and performed imaging mass cytometry on MF skin tissue. This visualized the structure of MF skin and the distribution of $CD4^+$ T cells, regulatory T-cells, $CD8^+$ T cells, malignant T cells, and various myeloid cell subsets. We observed clusters of $CD4^+$ T cells and multiple types of dendritic cells (DCs) identified through differential expression of CD11c, CD1a and CD1c in the dermis. These results indicate substantial heterogeneity in the composition of the local immune infiltrate but suggest a prominent role for clustered CD4-DC interactions in disease pathogenesis. Probably, the local inhibition of such interactions may constitute an efficient treatment modality.

Key terms: Mass cytometry; CyTOF; imaging mass cytometry; IMC; mycosis fungoides; Cutaneous T-cell Lymphoma; CTCL

Introduction

Mycosis fungoides (MF) is the most common variant of cutaneous T-cell lymphoma (CTCL), with a 5 years disease specific survival around 80% depending on the stage of the disease[1, 2]. The majority of MF patients have early stage disease (Stage IA/IB), with red scaly (sometimes itchy) patches and plaques on the skin with no extracutaneous involvement. Early stage MF can be extremely subtle, with skin lesions only present on a small body area. Those lesions are hard to recognize by untrained physicians and can be easily confused clinically as well as histologically with reactive dermatitis, leading to a diagnostic delay and mistreatment[3, 4]. Definite diagnosis is made by the clinicopathological correlation and sensitive for error. Therefore, the need of adjuvant diagnostic tools is desirable.

Histologically, early stage MF is characterized by small- to medium-sized pleomorphic T-cell lymphocytes with cerebriform nuclei infiltrating the basal layer of the epidermis (epidermotropism)[5]. However, the characteristic tumor cells in early stage MF can be scarce and hard to recognize. Immunophenotyping, to document loss of T cell antigens suggestive for a malignancy (CD3, CD5, CD7), and to determine the phenotype of the malignant cells (CD4, CD8, cytotoxic markers), can be of help. Still the diagnosis of early stage MF remains challenging, since early-stage MF lesions are characterized by a low number of tumor cells and an extensive inflammatory infiltrate with a relative abundance of $CD8^+$ T cells and dendritic cells (DCs). Multiple studies suggest that complex loops of cytokine and chemokine signaling between fibroblasts, keratinocytes and malignant T cells contribute to an inflammatory microenvironment that contribute to the progression of disease. These studies suggested that a decrease in $CD8^+$ T-cells and an increase in inhibitory M2 macrophages, combined with a shift from Th1 to Th2-dominated microenvironment, and alteration of the regulatory T-cell (Treg)/ Th17 balance lead to progression of MF. Furthermore the viability and growth of the malignant T-cells seemed partly dependent on interaction with immature dendritic cells, through contact between CD40 located on dendritic cells and CD40 ligand located on malignant T-cells[6]. Another in vitro study further supported previous observation, in which dendritic cells stimulates cultures of malignant T-cells and induces Treg cytokine production[7]. However, comprehensive studies investigating the different subsets of immune cells in tissue context are largely lacking, and little is known about cell-cell interactions between tumor cells and the reactive immune infiltrate.

Recently, single cell phenotyping platforms, such as single-cell RNA sequencing

and mass cytometry (cytometry by time-of-flight; CyTOF) have been utilized to investigate cellular heterogeneity[8, 9], to identify novel cellular subsets[10, 11], and to discover clinical relevant biomarkers with clinical value in human[12]. Mass cytometric techniques can characterize different immune cell populations in dissected skin cells and in the tissue contexture[13, 14]. Single cell mass cytometry allows an unbiased analysis of the complexity and heterogeneity of the human immune system as over 40 unique cellular markers can be measured simultaneously[15, 16]. In addition, imaging mass cytometry, which couples a laser ablation system with a mass cytometer, allows for the analysis of up to 40 markers in a single tissue section. With imaging mass cytometry, tissue structures can be visualized as well as the composition, distribution and spatial interactions of the stromal and immune cell subsets in the tissue context[17, 18].

In the current study, we applied single cell suspension and imaging mass cytometry to skin biopsies of early stage MF patients to gain deeper insight into the composition and organization of the immune compartment in the tissue context and the relation/interaction with malignant T-cells. We observed pronounced patient-specific characteristic features in the skin resident immune populations, and distinct clusters of lymphoid and myeloid cell populations in lesional skin that may drive the transformation and subsequent sustenance of the tumor cells in *situ*.

Material and methods

Patient selection

A total of 16 skin biopsies (4mm) with confirmed diagnoses of early stage MF (stage IA/IB; patches/plaques, no tumors) and 21 biopsies of normal skin (NS) were selected from the "Biobank Dermatology" of the Leiden University Medical Center. All biopsies were taken from the lesions of MF patients that were not previously treated with topical steroids, and the MF patients had not received any systemic medication yet at time of biopsy. All diagnoses had been confirmed by an expert panel of dermatologists and pathologists of the Dutch Cutaneous Lymphoma Group. An additional biopsy from the same lesion and photographic documentation were available for routine diagnostics and determination of the subtype of MF (i.e. Folliculotropic MF, $CD8^+$ MF). Approval by the medical ethical commission of the Leiden University Medical Center (protocol B19.005) was obtained in accordance with the local ethical guidelines and the Declaration of Helsinki. All patient provided written informed consent for biobanking. Baseline characteristics and disease course during follow-up are given in table S1, and the

sex and age characteristics of the NS donors are shown in table S2.

Skin biopsy processing

The fresh skin biopsies (MF, n=10; NS, n=17, for suspension mass cytometry) and the snap-frozen biopsies (MF, n=6; NS, n=4, for imaging mass cytometry) were retrieved from the biobank. Fresh skin punch biopsies were maintained in cold HBSS solution and brought to the laboratory within 10 - 30 mins. To obtain single cell suspensions, the skin biopsies were cut into small pieces and transferred to a gentleMACS C tube to incubate in 500 µl IMDM (Lonza, Basel, Switzerland) supplemented with 10% FCS, 1 mg/ml collagenase D (Roche Diagnostics), and 50 µg/ml DNase I (Roche Diagnostics, Basel, Switzerland), at 37°C for 2 hours, after which 500 µl of IMDM with 10% FCS was added to terminate digestion. Subsequently the gentleMACS program h_skin in gentleMACS™ Dissociator (Miltenyi Biotec, Bergisch Gladbach, Germany) was run after which the cells were spun down. Finally, cell suspensions were filtered through a 70-µm nylon cell strainer and immediately stained with the single-cell mass cytometry antibody panel. Snap-frozen skin tissues were obtained by embedding in optimal cutting temperature compound (O.C.T., VWR), frozen in cold isopentane (VWR) and store in -80° C for immunodetection staining by IMC.

Suspension mass cytometry antibody staining and data acquisition

Metal-conjugated antibodies used for single-cell mass cytometry are listed in Table S3. For self-conjugation of antibodies, BSA-free and carrier-free formulations of antibodies were purchased from different suppliers. Subsequently, conjugation of antibodies with lanthanide metals was performed using the MaxPar Antibody Labeling Kit (Fluidigm, San Francisco, CA, USA) following the manufacturer's instructions. Post-conjugation, all antibodies were eluted in 100 µl W-buffer (Fluidigm) and 100 µl antibody stabilizer buffer (Candor Bioscience) supplemented with 0.05% sodium azide. Procedures for mass cytometry antibody staining and data acquisition were performed as previously described[19]. In short, skin cells were incubated with 1 ml 250 µM Cell-ID™ intercalator-103Rh (Fluidigm) for 15 min at room temperature (RT) to distinguish live cells from dead cells in 5 ml microcentrifuge tubes. After washing once by by Maxpar® Cell Staining Buffer (Fluidigm), the skin cells were stained with metal-conjugated antibodies for 45 min at RT (Table S3). After staining and washing by Maxpar® Cell Staining Buffer (Fluidigm) for three times, cells were incubated with 1 ml 2000× diluted 250 µM Cell-ID™ intercalator-Ir (Fluidigm) in MaxPar Fix and Perm Buffer (Fluidigm) overnight at 4° C. The next day, skin cells were washed by Maxpar® Cell Staining Buffer (Fluidigm) for 3 times and spun down. Finally, cells were acquired on a

Helios time-of-flight mass cytometer (Fluidigm). Data were normalized by using EQ Four Element Calibration Beads (Fluidigm) with the reference EQ passport P13H2302 in each experiment.

Imaging mass cytometry staining and Data acquisition

Procedures for IMC antibody staining and data acquisition for snap-frozen tissue were carried out as previously described[20]. In short, snap-frozen human skin biopsies were sectioned at a thickness of 5 µm. All tissue sections were dried for 1 hour at RT after cutting, then were fixed by incubating with 1% paraformaldehyde (PFA) for 5 min at RT followed by 100% methanol for 5 min at -20° C. After fixation procedures, tissue sections were washed in Dulbecco's phosphate-buffered saline (DPBS, ThermoFisher Scientific, Waltham, MA, USA) with 1% bovine serum albumin (BSA, Sigma) and 0.05% Tween, rehydrated in additive-free DPBS. After washing, the tissue sections were blocked by Superblock Solution (ThermoFisher Scientific) for 30 min in a humid chamber at RT. Tissue sections were then stained with 36 antibodies mixture overnight at 4° C, all antibodies of IMC panel were listed in Table S4. After antibody mixture incubation, the tissue sections were washed and incubated with 125 nM Cell-ID^{Tm}Intercalator-Ir for 30 min at RT. After an additional wash, tissue sections were washed by Milli-Q water (Merck Millipore) for 1 min to remove additives and dried for 20 min at RT. The acquisition was performed by a UV-laser spot by-spot of Hyperion Imaging System at a resolution of 1 µm and a frequency of 200 Hz. Regions of interest (ROIs) with 1000 µm × 1000 µm or 1200 µm × 1000 µm were selected in skin tissue sections. We ablated the whole skin tissue section by 1 to 2 ROIs to cover the whole skin biopsy sections. After ablation by Hyperion (Fluidigm) as described in the Hyperion imaging system user guide, MCD files and txt files were generated for each sample for further analysis.

Data Analysis

Data for single, live CD45$^+$ cells were gated from each MF sample individually using Flowjo software as shown in Figure S1A. Subsequently, the data were sample tagged and hyperbolic arcsinh transformed with a cofactor of 5 and subjected to dimensionality reduction analysis in Cytosplore^{+HSNE}[15, 16]. We employed a 43-antibody panel for staining of single cell mass cytometry (Table S3). Major immune lineages were identified at the overview level of a hierarchical stochastic neighbor embedding (HSNE) analysis on CD45$^+$ cells data from all samples with default perplexity (30) and iterations (1000). All HSNE and t-SNE plots were generated in Cytosplore[15, 16]. The immune lineage population frequencies of CD45$^+$ cells were computed within the individual samples using the "prcomp" function, and the result was visualized using the "ggbiplot" function in R software. Hierarchical

clustering of the phenotype heatmap was created with Euclidean correction and average linkage clustering while the cell frequency heatmap with Spearman correction and average linkage clustering was generated in Matlab R2016b.

We utilized a 36-antibody panel for staining of IMC on snap-frozen skin tissue to visualize spatial data (Table S4). All IMC raw data were from three independent experiments and analyzed by using the Fluidigm MCD™ viewer (v1.0.560.2). The images of single marker within IMC panel are shown in Figure S5 to S14, to show the individual stains in each NS and MF sample. And the minimum and maximum threshold of each marker for all samples were provided as Table S5, in which the maximum threshold value reflects the staining density of the antibodies, while the minimum threshold value was used to reduce the background signal for each marker-channel. To combine related markers to visualize structure of skin tissue and distinct immune subsets, we utilized the Fluidigm MCD™ viewer to generate the images for a single ROI of skin tissue.

Results

Identification of Major Immune Lineages

We applied a 43-antibody panel to identify the major immune lineages ($CD4^+$ T cells, $CD8^+$ T cells, myeloid cells, B cells and innate lymphoid cells (ILCs)) in 10 early stage MF patients. This antibody panel contained markers for identification of the immune lineages, cellular differentiation, activation, trafficking, tissue residency and function (Table S3). Single, live $CD45^+$ cells were selected by means of DNA and CD45 staining, and commonly used mass cytometry parameters (Figure S1A). From the skin biopsies we acquired on average 1737 $CD45^+$ cells from normal skin (NS), and 16396 $CD45^+$ cells from MF skin by single-cell mass cytometry (Figure 1A). In agreement, IMC analysis revealed substantial immune cell infiltration in *situ* in MF patients in comparison with NS samples (Figure 1B). Due to much lower amount of immune cells detected on NS samples by both techniques, we next focused on MF patients for further analysis.

To analyze the composition of the immune cell infiltrate of MF patients, we integrated the data derived from 10 MF samples (3.6×10^5 $CD45^+$ cells), and performed a HSNE analysis in Cytosplore^{+HSNE} at the global level to identify the major immune lineages (Figure 2A). Based on the marker expression profiles (Figure 2B) and density features of the embedded cells (Figure S1B), we identified clusters of $CD3^+CD4^+$ T cells, $CD3^+CD8^+$ T cells, $CD11c^+/CD11b^+$ myeloid cells, $CD3^-CD20^-CD11c^-CD11b^-CD7^+$ innate lymphoid cells (ILCs), $CD20^+$ B cells and

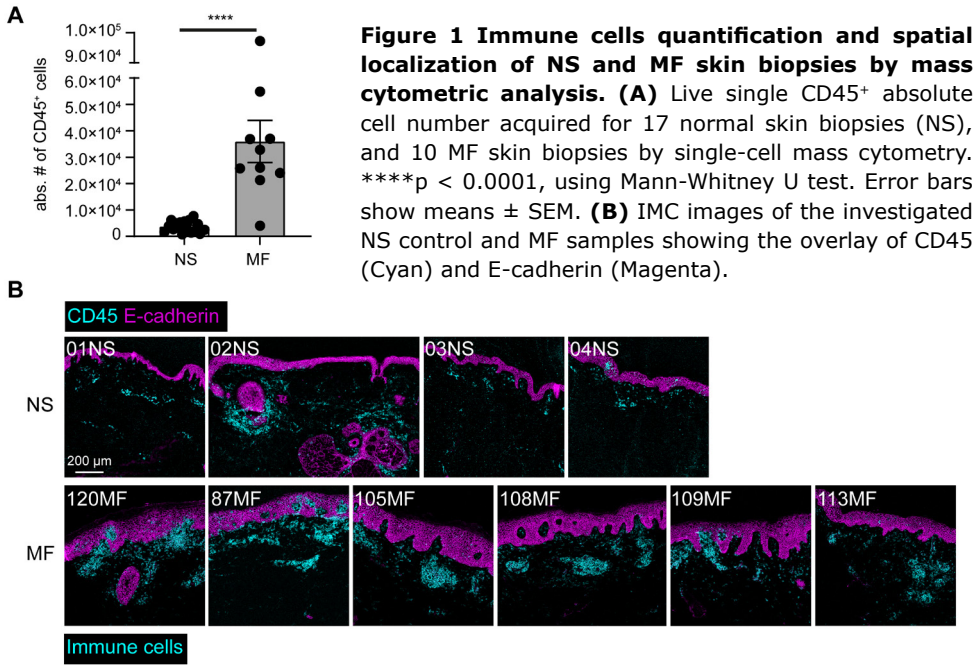

Figure 1 Immune cells quantification and spatial localization of NS and MF skin biopsies by mass cytometric analysis. (A) Live single CD45$^+$ absolute cell number acquired for 17 normal skin biopsies (NS), and 10 MF skin biopsies by single-cell mass cytometry. ****p < 0.0001, using Mann-Whitney U test. Error bars show means ± SEM. **(B)** IMC images of the investigated NS control and MF samples showing the overlay of CD45 (Cyan) and E-cadherin (Magenta).

abnormal CD3$^-$CD7$^-$CD8$^-$CD4$^+$ T cells (Figure 2A, S1B). Moreover, we quantified the relative frequencies of these major immune lineages within the CD45$^+$ cells of each MF patient (Figure 2C). We observed that CD3$^+$CD4$^+$ T cells were the dominant cell population in MF patients as they represented more than 50% of CD45$^+$ cells in eight out of ten MF patients. Both CD3$^+$CD8$^+$ T cells and myeloid cells were present in all patients, but their percentage varied significantly among patients. In five out of ten patients aberrant T cells with loss of CD3 and CD7 expression (CD3$^-$CD7$^-$CD8$^-$CD4$^+$ T cells) were observed. This aberrant phenotype was most prevalent in patient 79MF but lower in the other 4 patients (84MF, 82MF, 81MF, 62MF). Significant numbers of CD3$^-$CD20$^-$CD11c$^-$CD11b$^-$CD7$^+$ ILCs were only detected in three patients while only few B cells being present in all patient samples. Together, these global analyses revealed that all major immune lineages could be readily identified in MF patients, and that the composition of these immune cells differed among the evaluated patients.

Analysis of the CD4 T cell compartment reveals shared and patient-unique features

To define and compare the composition of the T cell immune compartment between MF samples, we next selected the T cell clusters individually and performed a tSNE analysis at the single-cell level. The embedding of the CD3$^{+/-}$CD4$^+$ T cells indicated

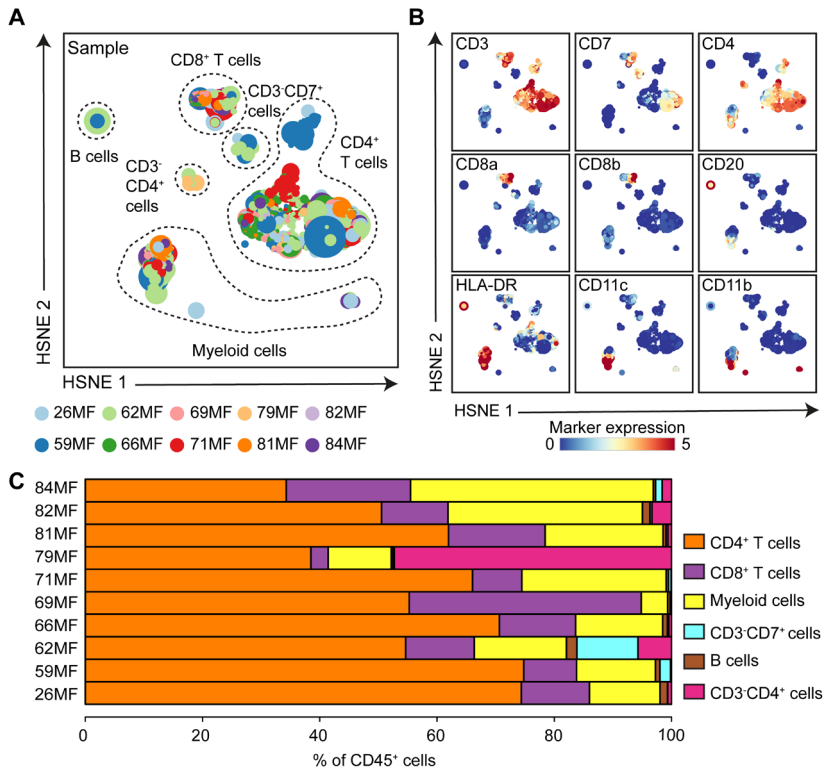

Figure 2 HSNE analysis reveals major immune lineages across MF patients. (A, B) HSNE embedding showing 6.9×10^4 landmarks representing all immune cells (3.6×10^5 cells) isolated from fresh skin biopsies of MF patients (n=10) at the overview level. Each dot represents a HSNE landmark and the size of the landmark indicates the number of cells that each landmark represents. Colors represent the individual MF patients (A) and the related expression level of indicated immune markers (B). **(C)** The composition of major immune lineage populations of $CD45^+$ cells in the individual MF patient is represented in horizontal bars where the colored segment lengths represent the proportion of cells as a percentage of $CD45^+$ cells in the sample. Colors represent the different major immune lineage population.

that next to shared features (encircled in gray, Figure 3A), distinct clusters of cells that were highly enriched in individual patients were also readily identified (encircled in black, Figure 3A). Based on the density features and related marker expression profiles of the t-SNE-embedded cells (Figure 3B, S2), we identified 27 distinct $CD4^+$ T cell clusters, each defined by a unique marker expression profile (Figure 3C). The associated cell frequency heatmap gave an overview of the relative abundance of those subsets in the patient samples (Figure 3D).

Unsupervised hierarchical clustering of the patient samples based on the cell frequency heatmap grouped 6 samples together while the other 4 samples were distinct (Figure 3D, top). Visual inspection of the heatmap indicated that the

clustering of the 6 samples was to a large extent due to the sharing of clusters CD4 T-2, CD4 T-6 and CD4 T-7, and to a lesser extent by CD4 T-1 and CD4 T-4 (Figure 3D, pink boxes), which was confirmed by the actual percentage of these subsets in the individual patient samples (Figure 3E). The actual percentage of these subsets in the individual patient samples support the notion that cluster CD4 T-1 and CD4 T-4 ($CD3^+CD5^+CD127^+CD45RO^+CCR7^-$ Effector memory) and CD4 T-2 ($CD3^+CD5^+CD127^-CD45RO^+CD25^+$ Treg-like) were the most important in this respect (Figure 3E). In contrast, the remaining 4 patient samples were distinguished by the presence of distinct clusters of CD4 T cells (Figure 3D, black boxes) that were either $CD3^+$ or $CD3^-$ and many of which display variable expression levels of CD30 and CLA (Figure 3C) and thus likely contain the abnormal cells in these patients. Here patient 62MF was typified by the presence of CD4 T-26 and T-27 ($CD3^-CD103^{+/-}CD26^+CD30^{low}CD5^+CD127^+PD1^+CD69^+CD45RO^+$), patient 71MF by cluster CD4 T-15, T-18 and T-28 ($CD3^+CD103^{+/-}CD30^{low}CLA^{low}CD5^+PD1^+CD69^+CCR4^+CCR7^+CD28^+CD45RO^+$), patient 79MF by cluster CD4 T-11 , T-14 ($CD3^{+/-}CD26^+CD30^+CLA^+CD25^{low}CD5^+CD127^{+/-}CD69^+CD28^+CD45RO^+$) and cluster CD4 T-16 ($CD3^-CD26^+CD5^-CD127^-CD69^+CD28^-CD45RO^+$), patient 59MF by cluster CD4 T-23 and T-24 ($CD3^-CD161^+CD26^+CD30^{+/-}CLA^{+/-}CD127^+CD103^{+/-}PD1^+CD69^+CCR6^+CD45RO^{+/-}$) and cluster CD4 T-21, CD4 T-22 ($CD3^+CD161^+CD103^{low/-}CD30^-CD127^{low}CLA^{+/-}CCR4^+CD28^-CCR7^+$) (Figure 3C). The actual percentages of these cell clusters in the individual patients underscores that these were the dominant cell type in the investigated biopsies (Figure 3F). In particular, the dominance of clusters in patients 71MF, 79MF and 59MF is striking where patient 79MF is distinct as it was the only one harboring a large population of $CD3^-CD30^+CD5^+CD4^+$ T cell (cluster CD4 T-11) (Figure 3D, 3F).

A similar analysis of the $CD8^+$ T cells showed that the distribution $CD8^+$ T cells was highly similar in nine out of ten patients (Figure S3A). Based on marker expression profiles and density feature, 25 $CD8^+$ T cell clusters were identified (Figure S3B-C). We observed that hierarchical clustering resulted in three patient groups (Figure S3D) while 71MF patient was separate, due to a high proportion of cluster CD8 T-26 and T-27 ($CD103^+CLA^+PD\text{-}1^+$) (Figure S3D).

In conclusion, hierarchical clustering of the T cell compartment revealed both shared and unique features of the MF patients, where the shared features may relate to an earlier disease state while the appearance of highly patient-specific cell clusters is probably related to evolution and the response of the tumor microenvironment.

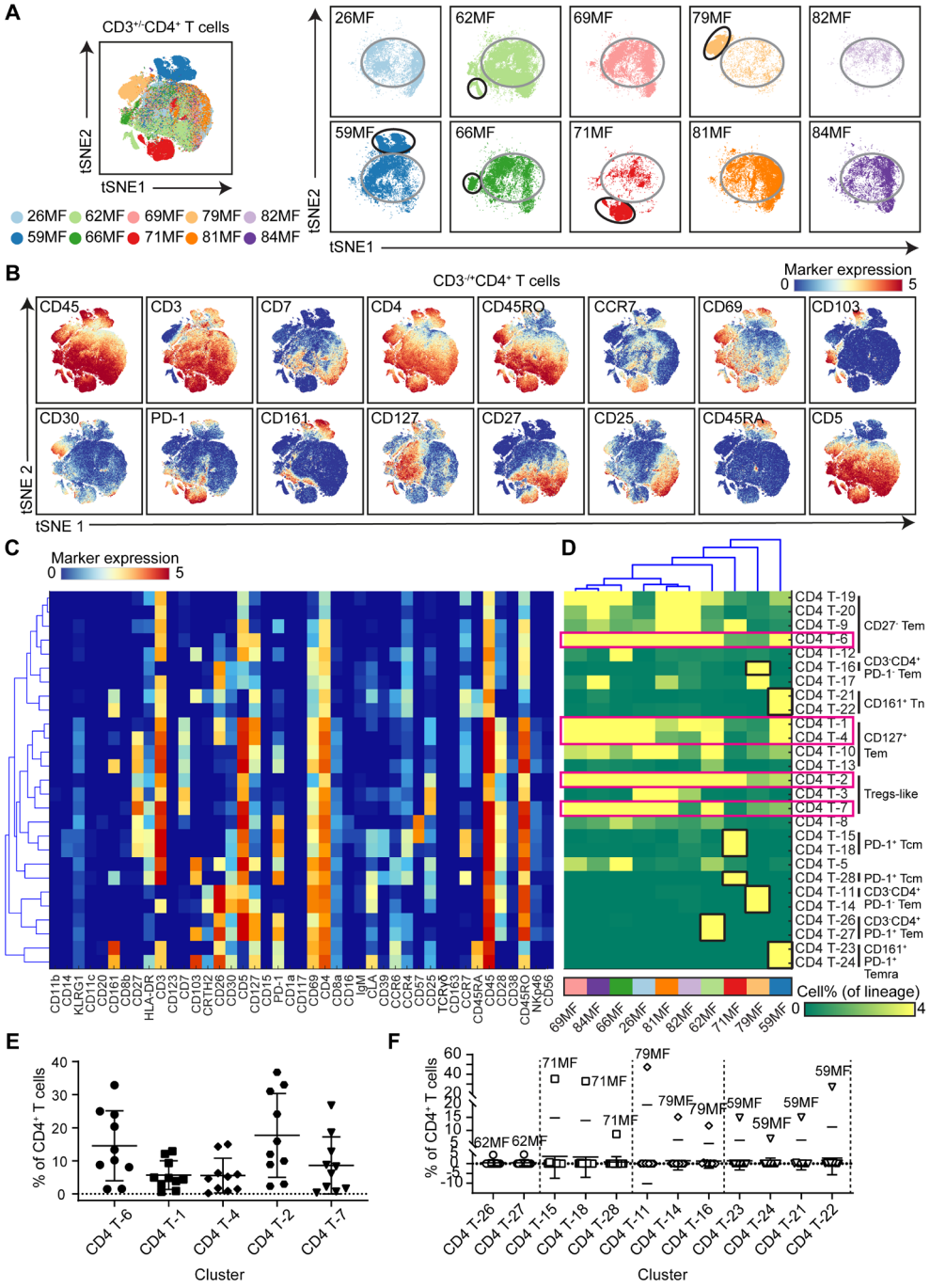

(Figure legend in next page)

Figure 3 Identification of phenotypically distinct clusters in the CD3$^{+/-}$CD4^{+} T cell compartment across MF samples. (A) A collective t-SNE was performed on CD4^{+} T cells (CD3^{+}CD4^{+} T cells and CD3^{-}CD4^{+} T cells) and stratified for samples (n = 10). In total, 2.3×10^{5} CD4^{+} T cells were analyzed in the plots. The large encircled cluster of cells (encircled in gray) harbors cells exhibiting a similar phenotype in all patients. The smaller cell clusters encircled in black are patient-unique and likely contain the abnormal cell populations in these patients. **(B)** Relative expression level of indicated immune markers. Colors represent different level of marker expression. **(C)** Heatmap showing the median of the marker expression values for the clusters identified and hierarchical clustering thereof. **(D)** Heatmap showing the corresponding cell frequencies of identified clusters of total CD4^{+} T cells in each sample. Colors represent different MF samples as indicated below the heatmap. The dendrogram shows the hierarchical clustering of samples. The clusters of CD4^{+} T cells highlighted by pink boxes are shared by the majority of MF patients. The clusters of cells highlighted by black boxes are unique for the individual patients. **(E)** Quantification of the shared CD4^{+} T cells clusters frequencies among samples in (C). Cluster IDs correspond to the ones in (C). **(F)** Quantification of the patient-unique CD4^{+} T cells clusters frequencies among samples in (C). Cluster IDs correspond to the ones in (C).

Analysis of the myeloid compartment reveals shared and patient-unique features

We next analyzed the myeloid compartment. Similar to the CD4^{+} T cells, the tSNE analysis revealed the presence of subsets that are overrepresented in particular MF patients (Figure 4A, patients 26MF, 62MF, 71MF and 84MF, encircled). Based on the distribution of the markers expression profiles (Figure 4B) and the density features of the t-SNE-embedded cells (Figure S4), 28 distinct myeloid cell clusters were identified that fall within 6 major clusters (CD11c^{dim}HLA-DR^{+} myeloid cells, CD11c^{-}HLA-DR^{+} cells, CD14^{+} monocytes, CD16^{+}CD15^{dim} monocytes, HLA-DR^{+}CD1a^{+}dendritic cells and CD163^{+} macrophages) (Figure 4C).

Figure 4 Identification of phenotypically distinct clusters in the myeloid cell compartment across MF samples. (A) A collective t-SNE was performed on myeloid cells and stratified for samples (N = 10). The plots are showing in total 6.1×10^{4} myeloid cells. The islands encircled in black are the unique-patient clusters of myeloid cells. **(B)** Relative expression level of indicated markers. Colors represent different level of marker expression. **(C)** Heatmap showing the median of the marker expression values for the clusters identified and hierarchical clustering thereof. **(D)** Heatmap showing the corresponding cell frequencies of the identified clusters as a percentage of total myeloid cells in each sample. Colors represent different samples as indicted below the heatmap. The dendrogram shows the hierarchical clustering of the samples. The clusters of myeloid cells highlighted in pink boxes are shared by the majority of MF patients. The clusters of myeloid cells highlighted in black boxes are patient-unique. **(E)** Quantification of the shared myeloid cells clusters frequencies among samples in (C). Cluster IDs correspond to the ones in (C). **(F)** Quantification of the patient-unique myeloid cells clusters frequencies in (C). Cluster IDs correspond to the ones in (C).

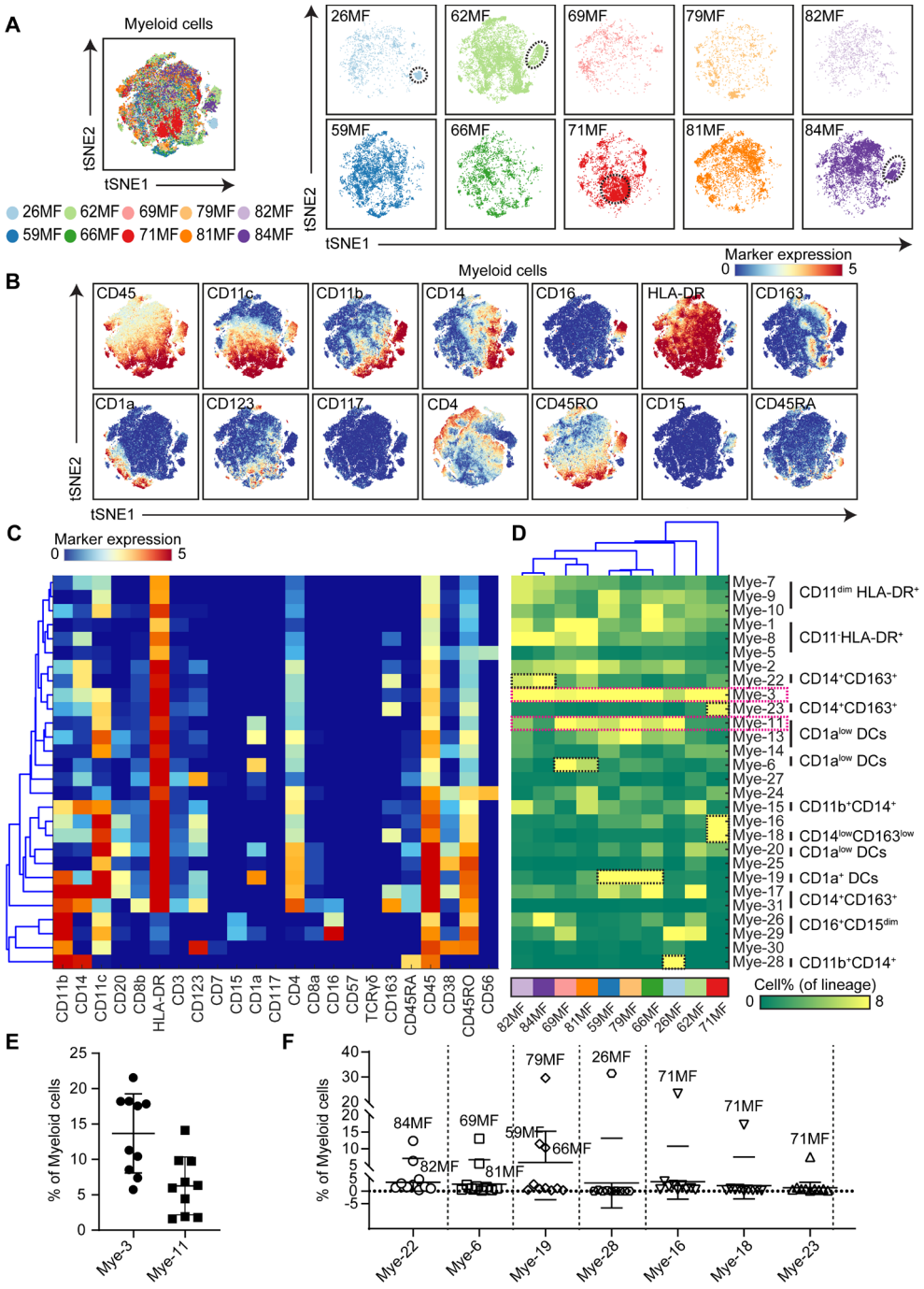

(Figure legend in previous page)

Compared to the $CD4^+$ T cells, the myeloid cell associated cell frequency heatmap was much more complex and indicative of much heterogeneity (Figure 4D). However, the subset Mye-3 ($CD11b^{low}CD11c^+CD14^{dim}$HLA-$DR^+CD4^{low}$) was present in all MF patients (Figure 4D, pink box), and cluster Mye-11 ($CD11b^-CD11c^+$HLA-$DR^+CD1a^{dim}CD4^{low}$) was also observed in the majority of MF patients (Figure 4D, pink box and 4E), while cluster Mye-19 ($CD1a^+CD11b^+CD11c^+$HLA-DR^+) marked patients 79F, 59MF and 66MF (Figure 4D, black box and 4F). In contrast, cluster Mye-28 ($CD11b^+CD11c^-CD14^+CD45RA^+CD163^-$HLA-$DR^-$) was essentially only present in patient 26MF and cluster Mye-16, 18 and 23 ($CD11b^{low/-}CD11c^+$HLA-$DR^+CD163^{+/-}$) only in 71MF (Figure 4D, black boxes and 4F). Finally, patient 82MF and 84MF shared cluster Mye-22 ($CD11b^-CD11c^-CD14^+$HLA-$DR^+CD163^+CD4^{low}$), and patient 69MF and 81MF shared cluster Mye-6 ($CD11b^-CD11c^-$HLA-$DR^+CD1a^+CD4^{low}$) (Figure 4D, black boxes and 4F). Thus, similar to the $CD4^+$ T cell compartment, the analysis of the myeloid compartment also revealed both shared and unique features of the MF patients that may relate to different stages of disease progression. Here it is important to note that in some patients (71MF, 79MF, and to a lesser extent 69MF and 59MF) both patient-unique $CD4^+$ T and myeloid cell populations were observed.

Imaging Mass Cytometry Reveals the Spatial Signatures in *situ*

To determine the spatial distribution of the immune and stromal cells in *situ* we applied an IMC panel comprising 36 antibodies to tissue sections of NS and MF skin biopsies. The antibody panel contained markers to visualize the overall tissue architecture such as E-Cadherin (epithelium), vimentin (intermediate filament), α-smooth muscle actin (αSMA) and collagen I (extracellular matrix), and markers to identify T cells (CD3, CD8, CD4, CD25, FOXP3, CD45RA, CD45RO), B cells (CD20), NK cells (CD7 and CD56), myeloid cells (CD11c), dendritic cells (CD1a, CD1c, CD123 and CD141), mast cells (CD117 and FcεRIα), monocytes and macrophages (CD14, CD68, CD163 and HLA-DR). In addition, CD31 was included to identify endothelial cells and Ki-67 to identify cell proliferation (Table S4). With this panel, snap-frozen tissue sections derived from four NS controls, and six early stage MF patients were stained after which data were acquired on a Hyperion imaging mass cytometer.

To obtain further information on the phenotype and localization of the immune cell subsets within the tissue context, we visualized the data by combinations of specific markers (Figure 5, 6). Here, the combination of E-cadherin and DNA as nuclear counterstain were used to distinguish the epidermis from the dermis on skin tissues from the NS control and the MF patient (Figure 5A), while more

proliferating keratinocytes (the basal cells in the epidermis) were visualized at the junction between the epidermis and dermis by staining with Ki-67 in the MF sample, compared with the NS control sample (Figure 5B). Finally, vimentin, collagen I and CD45 revealed the localization of the immune cells in the epidermis and dermis, in the latter mostly enriched nearby blood vessels identified by expression of CD31 and αSMA for both samples (Figure 5C-D). In addition, we found several subregions with more infiltrating immune cells in the MF sample compared with the NS control, based on CD45 staining (Figure 5D). To define the spatial organization of the immune cells in more detail for MF patient, we next focused on the analysis of lymphoid and myeloid cell populations in the MF tissue sections. Representative images are shown in Figure 5 in which we identified $CD3^+CD7^+$ T cells, abnormal $CD3^+CD7^-$ T cells and $CD3^-CD7^+$ ILCs (Figure 5E-01), $CD3^+CD4^+$ T cells and $CD3^+CD8^+$ T cells in the dermis, and $CD3^+CD4^-CD8^-$T cells in the epidermis (Figure 5E-02). In addition, analysis of the expression of CD45RA, FOXP3 and CD25, revealed that the large majority of T cells had a memory phenotype and allowed the distinction between $CD45RA^-$ memory $CD4^+$ T cells (Figure 5E-03) and $FOXP3^+CD25^+$ Tregs (Figure 5E-04). Moreover, various myeloid cells subsets were detected (Figure 5F), including $CD11c^+CD1a^+CD1c^+$ DCs, $CD11c^+CD1a^-CD1c^+$ DCs, and $CD11c^+CD1a^-CD1c^-$ myeloid cells in the dermis; and $CD11c^-CD1a^+CD1c^+$ Langerhans-like cells (LCs) in the epidermis (Figure 5F-01), while $HLA\text{-}DR^+CD163^+$ macrophages were present in the dermis (Figure 5F-02). Also, we observed lower expression levels of HLA-DR in the epidermal LCs compared to dermal DCs (Figure 5F-03). Few $HLA\text{-}DR^+CD123^+$ pDCs-like cells were detected in the dermis (Figure 5F-04). Importantly, we observed prominent co-localization of $CD4^+$ T cells with both $CD1a^+CD1c^+$ and $CD1a^-CD1c^+$ DCs in cellular aggregates just below the epidermis. Thus, by this approach, we were able to identify and visualize the presence and distribution of various lymphoid and myeloid immune cell subsets within a single tissue section simultaneously.

We next analyzed five additional early stage MF patients which revealed similar clusters of immune cells just below the epidermis in all MF patients (Figure 6). Figure S5 to S10 provide an overview of the individual markers stains for all MF patients. The substantial heterogeneity of immune cells were observed among MF patients. While $CD4^+$ T cells were the most abundant lymphoid cells in patients 105MF, 109MF and 113MF, $CD8^+$ T cells were more abundant in patient 87MF and $CD4^-CD8^-$ T cells in patient 108MF (Figure 6A). Also, myeloid cells were virtually absent from the lymphoid cell aggregate in patient 87MF (Figure 6B) while co-localization of lymphoid cells and myeloid cells, in particular $CD11c^+CD1a^+CD1c^+$ DCs, was observed in patients 105MF and 109MF and to a lesser extent in patients

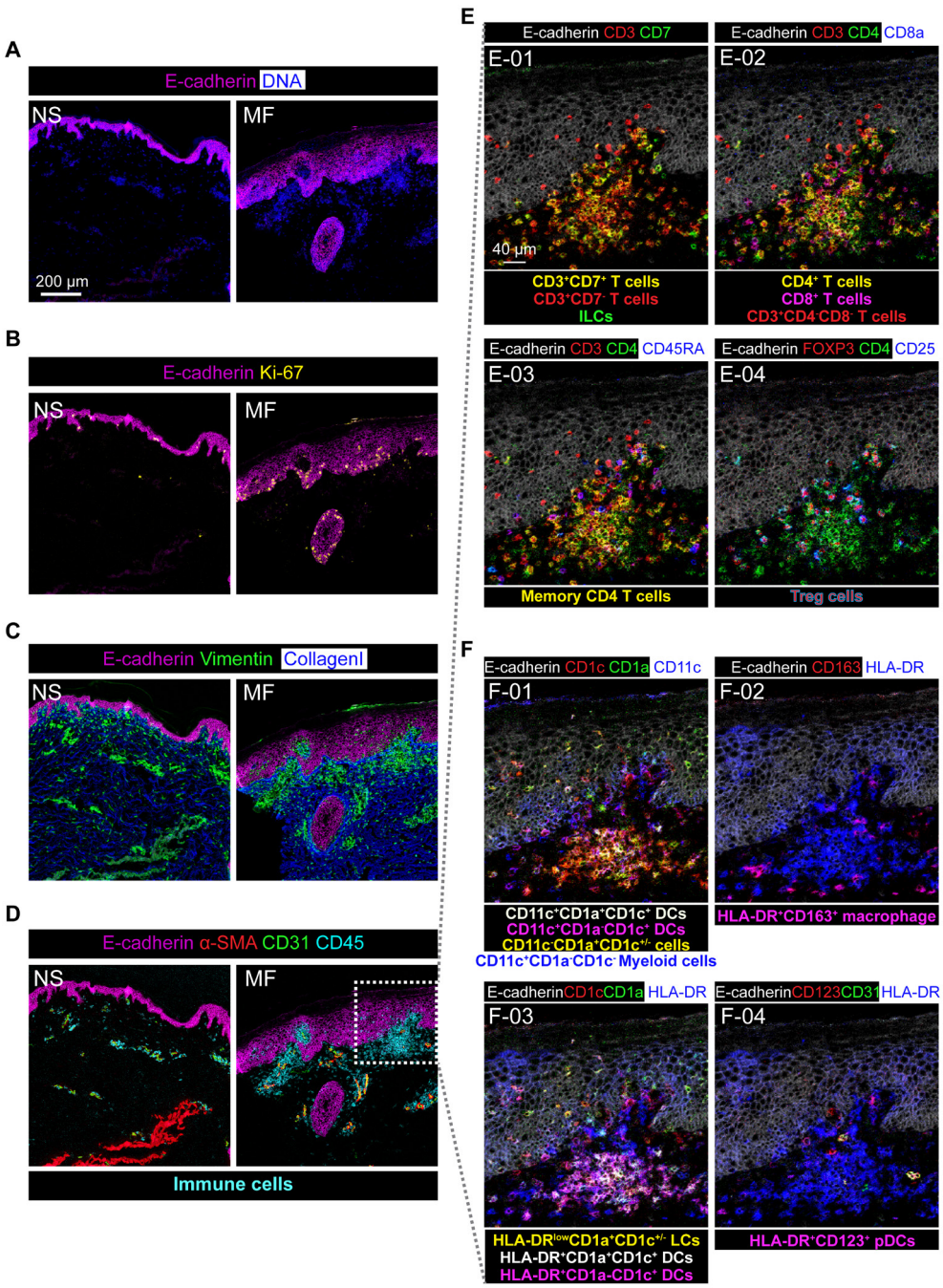

(Figure legend in next page)

Figure 5 Visualization of structure and the spatial distribution of the immune and stromal cell subsets in a single ROI in skin tissue by imaging mass cytometry. **(A-D)** Representative mass cytometry images of a NS and a MF skin sample showing the overlay of **(A)** E-Cadherin (colored in magenta) and DNA (colored in blue); **(B)** E-cadherin (colored in magenta) and Ki-67 (colored in yellow) to identify proliferating keratinocytes (E-Cadherin^{+}Ki-67^{+}); **(C)** E-cadherin (colored in magenta), Vimentin(colored in green) and Collagen I (colored in blue) to distinguish epidermis and dermis; **(D)** E-cadherin (colored in magenta), α-SMA (colored in red), CD31 (colored in green) and CD45 (colored in cyan) to show the location of CD45$^{+/dim}$ immune cells. **(E)** Identification of T cell and ILCs subsets for the MF sample : **(E-01)** CD3^{+}CD7^{+} T cells, CD3^{+}CD7^{-} T cells and ILCs (CD3^{-}CD7^{+}); **(E-02)** CD4^{+} T cells (CD3^{+}CD4^{+}), CD8^{+} T cells (CD3^{+}CD8^{+}) and CD4^{-}CD8^{-} T cells (CD3^{+}CD4^{-}CD8^{-}); **(E-03)** Memory CD4^{+} T cells (CD3^{+}CD4^{+}CD45RA^{-}); **(E-04)** Regulatory T cells (Tregs, CD3^{+}CD4^{+}CD25^{+}FOXP3^{+}). **(F)** Identification of myeloid cell, dendritic cells and macrophage subsets from the MF sample : **(F-01)** Different dendritic cells subsets based on different expression level of CD11c, CD1a and CD1c; **(F-02)** CD163^{+} macrophage (HLA-DR^{+}CD163^{+}); **(F-03)** Epidermal Langerhans cells (LCs, HLA-DR^{dim}CD1a^{+} CD1c^{+}), dendritic cells (DCs); **(F-04)** plasmacytoid dendritic cells-like cells (pDC-like, HLA-DR^{+}CD123^{+}).

108MF and 113MF (Figure 6C). Apart from patient 87MF, multiple types of antigen presenting cells were identified in all other patients based on differential expression of CD11c, CD1a and CD1c.

Together, this provides evidence that clusters of lymphoid and myeloid cells are found in the majority of early stage MF patients. Moreover, it reveals substantial heterogeneity in both the lymphoid and myeloid compartment within and among patients.

Discussion

In the current study we analyzed skin biopsies from early stage MF patients and healthy controls to characterize the complexity of the immune compartment using high-dimensional single-cell suspension mass cytometry and imaging mass cytometry. Compared with conventional flow cytometry and immunohistochemistry, these mass cytometry based techniques offer the opportunity to detect up to 40 cellular markers simultaneously, thus allowing a high resolution analysis of the immune compartment in the tissue context.

Figure 6 Detection of cell-cell interaction by combining T cell markers with myeloid cell markers in skin biopsies of five additional MF patients. **(A)** Visualization of CD4^{+} T cells, CD8^{+} T cells, and CD4^{-}CD8^{-} T cells. **(B)** Visualization of multiple types of antigen presenting cells (APCs) by the overlay of CD1c (colored in red), CD1a (colored in green), and CD11c (colored in blue). **(C)** The overlay of CD3 (colored in cyan), CD1c (colored in red), CD1a (colored in green), and CD11c (colored in blue) shows the distribution of the myeloid and T cell populations and complex interactions between those.

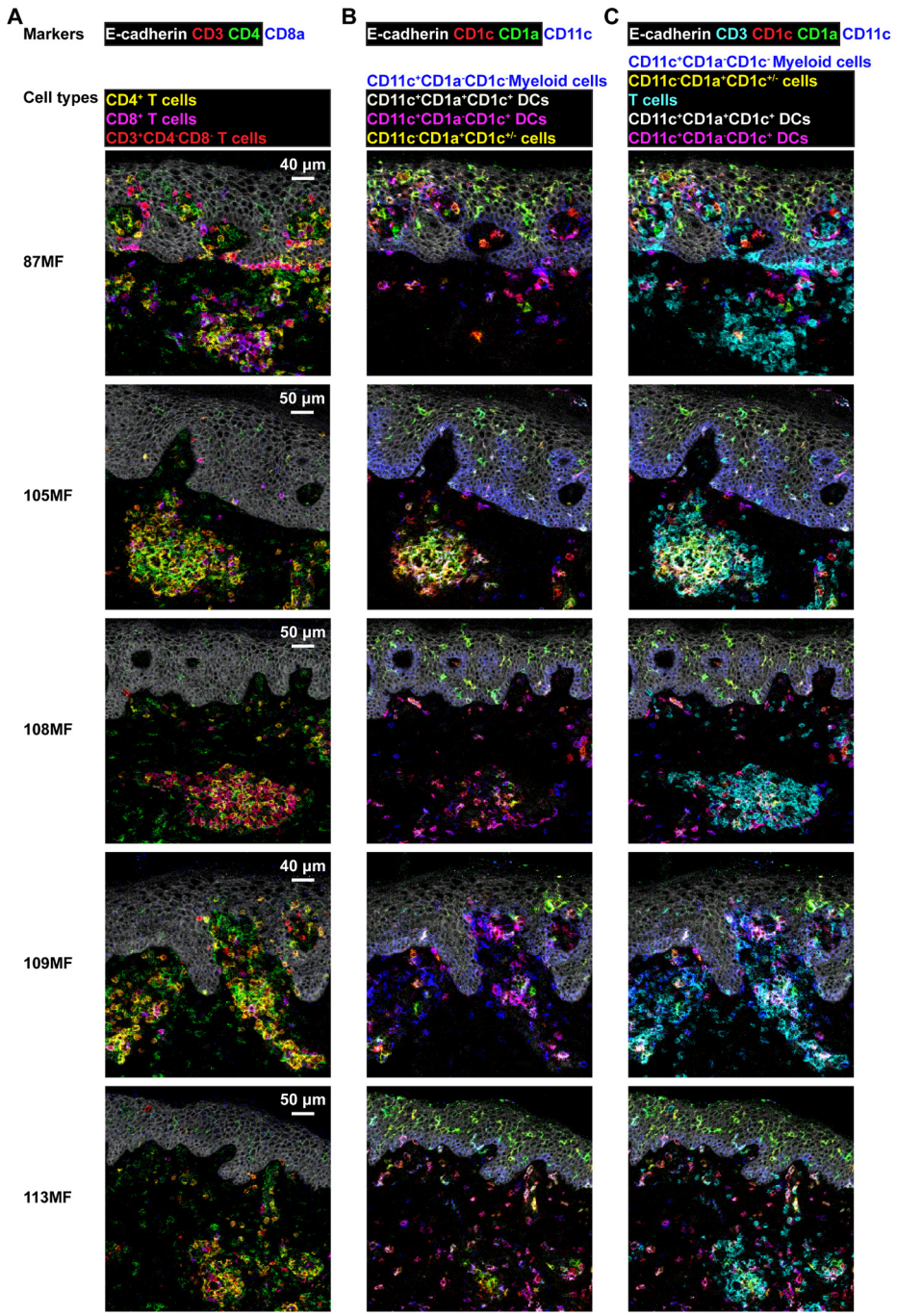

(Figure legend in previous page)

Previous studies found that early stages of MF were characterized by the presence of a small number of neoplastic cells together with an extensive inflammatory infiltrate composed of multiple types of immune cells[21, 22]. These observations have fueled the notion that this inflammatory response may contribute to the persistence and progression of MF lesions. In the present study we identified phenotypically distinct subsets in both the $CD4^+$ T cell and myeloid cell compartment that were shared by most patients. In addition, we found distinct $CD4^+$ T cell subsets that revealed an individual pattern, potentially representing a unique response of the tumor cells to the tumor microenvironment. In addition, substantial numbers of $CD4^+$ T cells co-localized with both $CD1a^+CD1c^+$HLA-DR^+ and $CD1a^-CD1c^+$HLA-DR^+ DCs in the dermis in *situ*. In this respect it is striking that the dominant presence of particular $CD4^+$ T cell clusters coincided with an elevated number of phenotypically distinct myeloid cells in some of the patients, suggesting that interactions between these $CD4^+$ T cells and myeloid cells may play a prominent role in disease control. Here it is of note that the composition, shape and organization of the lymphoid-myeloid cell aggregates differs substantially between patients. Future studies need to be performed to determine if this relates to disease progression and/or may have implications for therapy.

Previously, the studies focusing on Treg-like cells suggested that $FOXP3^+$ Tregs have a tumor suppressive role in the pathogenesis of MF/SS, but results have been discordant and conflicting[23, 24, 25]. In our single cell mass cytometry analysis clusters of Treg-like cells ($CD25^+CD45RO^+CD27^+$) were found in all patients. This observation was confirmed using imaging mass cytometry where $CD25^+FOXP3^+CD4^+$ T cells were found to be present in all investigated MF patients. Moreover, tumor-associated macrophages have been shown to generate an immunosuppressive tumor microenvironment by recruiting Tregs, myeloid cells and production of macrophage-related chemokines and angiogenic factors[26, 27, 28]. In patient 71MF, an increased number of $CD163^+$ macrophages were observed (Figure 4). Therefore, in future studies we will focus on the analysis of the interactions of the Tregs with myeloid and tumor cells in the tissue context. Here, future studies investigating the therapeutic effect of IFN-alpha and -gamma for immunomodulation of tumor associated macrophages might be of particular interest in such patients.

Finally, the PD-1/PD-L1 axis plays a central role in attenuating the immune response and antitumor immunity[29, 30] and has also emerged as a central tumor suppressor in T cell lymphomas[31]. We observed that PD-1 expression was higher in patients 71MF, 66MF and 59MF (Figure 3). However, due to the short follow-up time we could not observe a correlation between PD-1 expression and the disease

course. Future studies should investigate if the presence of PD-1^{+}CD4^{+} T cells correlates with progression to tumor stage disease. The therapeutic potential of PD-1 targeting therapy in these patients should be explored by investigating the factors driving PD-1 expression and functional consequences of PD-1 expression by CD4^{+} T cells as well.

In recent years, significant heterogeneity was observed between CTCL patients. Substantial clonotypic heterogeneity of skin- and blood-derived malignant T cells was observed by combining T-cell receptor clonotyping with cell surface marker profiling[32, 33, 34]. Moreover, genetic heterogeneity among and within CTCL patients was observed by TruSeq targeted RNA gene expression analysis[35]. These observations underscore the need to take into account the patients' individual malignant profiles for effective therapy of CTCL.

Moreover, among the various single cell techniques, cellular indexing of transcriptomes and epitopes by sequencing (CITE-seq) is a multimodal approach allowing simultaneous quantification of single-cell transcriptomes and surface proteins based on oligonucleotide-labeled antibodies of the same single cells[36]. Comparison of scRNA-seq, CyTOF and CITE-seq analyses, however, reveals discrepancies with the highest abundance of the T cell population in scRNA-seq analysis, followed by CyTOF and the lowest abundance in CITE-seq[37], pointing towards the need for further studies.

For future studies it would also be important to further optimize the antibody panels of single cell CyTOF for the detection of malignant T cells combined with detection of co-stimulatory signals (e.g. CD80)[38], immune modulatory signals (e.g. CD137, CD134 and CTLA4)[39, 40, 41], T cell exhaustion (e.g. ICOS)[42], and cytokine and chemokine receptors[43, 44], to further dissect the tumor microenvironment. In addition, while in the present study we have used the MCD™ viewer software to visualize the imaging mass cytometry data, this could be complemented with cell segmentation approaches based on the identification of nuclei to aid in the visualization of IMC data[45, 46]. Moreover, Imacyte[47] and Histocat[48], allow downstream imaging mass cytometry analysis to identify and quantify cell-cell interactions[49, 50]. Collectively, this allows for a further in-depth investigation of cellular interactions in skin tissues. Although the current study with a limited number MF patient needs to be expanded to confirm and extend the observations, we nonetheless demonstrate the ability to detect immune cell profile patterns in single cell suspensions of skin biopsies and visualize the spatial network in the tissue context. The identification of prominent cellular aggregates between CD4

T cells and myeloid cells in the dermis with a patient-unique cellular composition provides a framework for improving mycosis fungoides diagnosis and development of treatment tailored to the characteristic features of these aggregates in individual patients.

Supplementary Materials

The following supporting information can be downloaded at: https://www.mdpi.com/article/10.3390/cells11061062/s1, Figure S1: Gating strategy for single, live $CD45^+$ cells on MF samples (A), and identification of the overview level of $CD45^+$ cells by HSNE analysis (B). Figure S2: A collective t-SNE was performed on $CD3^-$ $CD4^+$ T cells and show the density map showing the local probability density of the embedded cells (left); Colors represent cluster partitions for per $CD4^+$ T cells subpopulation (right). Figure S3: Identification of phenotypically distinct clusters in the $CD3^+CD8^+$ T cell compartment across MF samples. Figure S4: A collective t-SNE was performed on myeloid cells. Figure S5-S14: Individual antibody stains for representative per skin sample by IMC. Table S1: Characteristics of patients with Mycosis fungoides diseases. Table S2: The sex and age characteristics of the NS healthy donors. Table S3: Single-cell suspension mass cytometry antibody panel. Table S4: Imaging mass cytometry antibody panel on frozen skin tissue. Table S5: The minimum and maximum threshold of each marker for per sample.

Author Contributions

N.G., M.V., F.K. and K.Q. conceived of the study and wrote the manuscript; N.G. performed most of the experiments with the help of L.J., C.O.-L. and N.F.C.C.d.M.; N.G. performed most of the analyses with the help of F.K., K.Q. and M.V.; K.Q., R.W. and M.V. obtained the fresh skin biopsies from the MF patients. All authors have read and agreed to the published version of the manuscript.

Funding

This research was supported by the China Scholarship Council (N.G. and L.J.). N.F.C.C.d.M. was funded by the European Research Council (ERC) under the European Union's Horizon 2020 Research and Innovation Programme (grant agreement no: 852832). F.K. was supported by BIOMAP (Bio-Markers in Atopic Dermatitis and Psoriasis), a project funded by the Innovative Medicines Initiative 2 Joint Undertaking (grant agreement no: 821511), and by the collaboration project TIMID (LSHM18057-SGF) financed by the PPP allowance made available by Top Sector Life Sciences & Health to Samenwerkende Gezondheidsfondsen (SGF) to stimulate public–private partnerships and co-financing by health foundations that are part of the SGF.

Institutional Review Board Statement

The study was conducted in accordance with the Declaration of Helsinki, and approved by the Medical Ethics Committee of Leiden University Medical Center (protocol: B19.005).

Informed Consent Statement

Informed consent was obtained from all subjects involved in the study.

Data Availability Statement

All data that support the findings of this study are available from the corresponding author upon reasonable request.

Acknowledgements

We thank the patients. We thank all operators in the Flow Cytometry Core Facility of the LUMC for technical assistance with measurements on Helios and Hyperion. We thank Marieke E. Ijsselsteijn from the Pathology department of the LUMC for providing help and suggestions in IMC experiments.

Conflicts of Interest

The authors declare no conflict of interest.

Reference

1. Willemze, R. *et al.* WHO-EORTC classification for cutaneous lymphomas. *Blood* **105**, 3768-3785 (2005).
2. Willemze, R. *et al.* The 2018 update of the WHO-EORTC classification for primary cutaneous lymphomas. *Blood* **133**, 1703-1714 (2019).
3. Reddy, K. & Bhawan, J. Histologic mimickers of mycosis fungoides: a review. *J Cutan Pathol* **34**, 519-525 (2007).
4. Chiba, T., Nagai, T., Osada, S.I. & Manabe, M. Diagnosis of Mycosis Fungoides Following Administration of Dupilumab for Misdiagnosed Atopic Dermatitis. *Acta Derm Venereol* **99**, 818-819 (2019).
5. Massone, C., Kodama, K., Kerl, H. & Cerroni, L. Histopathologic features of early (patch) lesions of mycosis fungoides: a morphologic study on 745 biopsy specimens from 427 patients. *Am J Surg Pathol* **29**, 550-560 (2005).
6. Berger, C. *et al.* The growth of cutaneous T-cell lymphoma is stimulated by immature dendritic cells. *Blood* **99**, 2929-2939 (2002).
7. Berger, C.L. *et al.* Cutaneous T-cell lymphoma: malignant proliferation of T-regulatory cells. *Blood* **105**, 1640-1647 (2005).
8. Gaydosik, A.M. *et al.* Single-Cell Lymphocyte Heterogeneity in Advanced Cutaneous T-cell Lymphoma Skin Tumors. *Clin Cancer Res* **25**, 4443-4454 (2019).
9. Li, N. *et al.* Early-Life Compartmentalization of Immune Cells in Human Fetal Tissues Revealed by High-Dimensional Mass Cytometry. *Frontiers in Immunology* **10** (2019).
10. Li, N. *et al.* Mass cytometry reveals innate lymphoid cell differentiation pathways in the human fetal intestine. *J Exp Med* **215**, 1383-1396 (2018).
11. de Vries, N.L. *et al.* High-dimensional cytometric analysis of colorectal cancer reveals novel mediators of antitumour immunity. *Gut* **69**, 691-703 (2020).
12. Havel, J.J., Chowell, D. & Chan, T.A. The evolving landscape of biomarkers for checkpoint inhibitor immunotherapy. *Nat Rev Cancer* **19**, 133-150 (2019).
13. Bandura, D.R. *et al.* Mass cytometry: technique for real time single cell multitarget immunoassay based on inductively coupled plasma time-of-flight mass spectrometry. *Anal Chem* **81**, 6813-6822 (2009).
14. Chang, Q. *et al.* Imaging Mass Cytometry. *Cytometry A* **91**, 160-169 (2017).
15. Hollt, T. *et al.* Cytosplore: Interactive Immune Cell Phenotyping for Large Single-Cell Datasets. *Comput Graph Forum* **35**, 171-180 (2016).
16. van Unen, V. *et al.* Visual analysis of mass cytometry data by hierarchical stochastic neighbour embedding reveals rare cell types. *Nat Commun* **8**, 1740 (2017).
17. Wang, Y.J. *et al.* Multiplexed In Situ Imaging Mass Cytometry Analysis of the Human Endocrine Pancreas and Immune System in Type 1 Diabetes. *Cell Metab* **29**, 769-783 e764 (2019).
18. Jackson, H.W. *et al.* The single-cell pathology landscape of breast cancer. *Nature* **578**, 615-620 (2020).
19. van Unen, V. *et al.* Mass Cytometry of the Human Mucosal Immune System Identifies Tissue- and Disease-Associated Immune Subsets. *Immunity* **44**, 1227-1239 (2016).
20. Guo, N. *et al.* A 34-Marker Panel for Imaging Mass Cytometric Analysis of Human Snap-Frozen Tissue. *Front Immunol* **11**, 1466 (2020).
21. Vermeer, M.H. *et al.* CD8+ T cells in cutaneous T-cell lymphoma: expression of cytotoxic proteins, Fas Ligand, and killing inhibitory receptors and their relationship with clinical behavior. *J Clin Oncol* **19**, 4322-4329 (2001).
22. Rubio Gonzalez, B., Zain, J., Rosen, S.T. & Querfeld, C. Tumor microenvironment in mycosis fungoides and Sézary syndrome. *Curr Opin Oncol* **28**, 88-96 (2016).
23. Gjerdrum, L.M. *et al.* FOXP3+ regulatory T cells in cutaneous T-cell lymphomas: association with disease stage and survival. *Leukemia* **21**, 2512-2518 (2007).
24. Tiemessen, M.M. *et al.* Lack of suppressive CD4+CD25+FOXP3+ T cells in advanced stages of primary cutaneous T-cell lymphoma. *J Invest Dermatol* **126**, 2217-2223 (2006).
25. Borcherding, N. *et al.* Single-Cell Profiling of Cutaneous T-Cell Lymphoma Reveals Underlying Heterogeneity Associated with Disease Progression. *Clin Cancer Res* **25**, 2996-3005 (2019).
26. Furudate, S. *et al.* Tumor-associated M2 macrophages in mycosis fungoides acquire immunomodulatory function by interferon alpha and interferon gamma. *J Dermatol Sci* **83**, 182-189 (2016).
27. Mendez-Enriquez, E. & García-Zepeda, E.A. The multiple faces of CCL13 in immunity and inflammation. *Inflammopharmacology* **21**, 397-406 (2013).
28. Tiemessen, M.M. *et al.* CD4+CD25+Foxp3+ regulatory T cells induce alternative activation of human monocytes/macrophages. *Proc Natl Acad Sci U S A* **104**, 19446-19451 (2007).
29. Francisco, L.M., Sage, P.T. & Sharpe, A.H. The PD-1 pathway in tolerance and autoimmunity. *Immunol Rev* **236**, 219-242 (2010).
30. Samimi, S. *et al.* Increased programmed death-1 expression on CD4+ T cells in cutaneous T-cell lymphoma: implications for immune suppression. *Arch Dermatol* **146**, 1382-1388 (2010).
31. Wartewig, T. & Ruland, J. PD-1 Tumor Suppressor Signaling in T Cell Lymphomas. *Trends Immunol* **40**, 403-414 (2019).

32. Iyer, A. *et al.* Clonotypic heterogeneity in cutaneous T-cell lymphoma (mycosis fungoides) revealed by comprehensive whole-exome sequencing. *Blood Adv* **3**, 1175-1184 (2019).
33. Hamrouni, A., Fogh, H., Zak, Z., Ødum, N. & Gniadecki, R. Clonotypic Diversity of the T-cell Receptor Corroborates the Immature Precursor Origin of Cutaneous T-cell Lymphoma. *Clin Cancer Res* **25**, 3104-3114 (2019).
34. Herrera, A. *et al.* Multimodal single-cell analysis of cutaneous T-cell lymphoma reveals distinct subclonal tissue-dependent signatures. *Blood* **138**, 1456-1464 (2021).
35. Litvinov, I.V. *et al.* Gene expression analysis in Cutaneous T-Cell Lymphomas (CTCL) highlights disease heterogeneity and potential diagnostic and prognostic indicators. *Oncoimmunology* **6**, e1306618 (2017).
36. Stoeckius, M. *et al.* Simultaneous epitope and transcriptome measurement in single cells. *Nature Methods* **14**, 865-868 (2017).
37. Yao, L. *et al.* Integrated Cytof, Scrna-Seq and Cite-Seq Analysis of Bone Marrow Immune Microenvironment in the Mmrf Commpass Study. *Blood* **136**, 28-29 (2020).
38. Zhang, Q. *et al.* Cutaneous T cell lymphoma expresses immunosuppressive CD80 (B7-1) cell surface protein in a STAT5-dependent manner. *J Immunol* **192**, 2913-2919 (2014).
39. Wong, H.K. *et al.* Increased expression of CTLA-4 in malignant T cells from patients with mycosis fungoides - Cutaneous T-cell lymphoma. *Journal of Investigative Dermatology* **126**, 212-219 (2006).
40. Kamijo, H. *et al.* Aberrant CD137 ligand expression induced by GATA6 overexpression promotes tumor progression in cutaneous T-cell lymphoma. *Blood* **132**, 1922-1935 (2018).
41. Jones, D., Fletcher, C.D., Pulford, K., Shahsafaei, A. & Dorfman, D.M. The T-cell activation markers CD30 and OX40/CD134 are expressed in nonoverlapping subsets of peripheral T-cell lymphoma. *Blood* **93**, 3487-3493 (1999).
42. Amatore, F. *et al.* ICOS is widely expressed in cutaneous T-cell lymphoma, and its targeting promotes potent killing of malignant cells. *Blood Adv* **4**, 5203-5214 (2020).
43. Lu, D. *et al.* The T-cell chemokine receptor CXCR3 is expressed highly in low-grade mycosis fungoides. *Am J Clin Pathol* **115**, 413-421 (2001).
44. Durgin, J.S., Weiner, D.M., Wysocka, M. & Rook, A.H. The immunopathogenesis and immunotherapy of cutaneous T cell lymphoma: Pathways and targets for immune restoration and tumor eradication. *J Am Acad Dermatol* **84**, 587-595 (2021).
45. Sommer, C., Straehle, C., Köthe, U. & Hamprecht, F.A. Ilastik: Interactive learning and segmentation toolkit. 2011 IEEE International Symposium on Biomedical Imaging: From Nano to Macro; 2011 30 March-2 April 2011; 2011. p. 230-233.
46. Jones, T.R. *et al.* CellProfiler Analyst: data exploration and analysis software for complex image-based screens. *BMC Bioinformatics* **9**, 482 (2008).
47. Somarakis, A., Van Unen, V., Koning, F., Lelieveldt, B. & Hollt, T. ImaCytE: Visual Exploration of Cellular Micro-Environments for Imaging Mass Cytometry Data. *IEEE Trans Vis Comput Graph* **27**, 98-110 (2021).
48. Schapiro, D. *et al.* histoCAT: analysis of cell phenotypes and interactions in multiplex image cytometry data. *Nature Methods* **14**, 873-876 (2017).
49. Ijsselsteijn, M.E., Somarakis, A., Lelieveldt, B.P.F., Hollt, T. & de Miranda, N.F.C.C. Semi-automated background removal limits loss of data and normalises the images for downstream analysis of imaging mass cytometry data. *bioRxiv*, 2020.2011.2026.399717 (2020).
50. Schulz, D. *et al.* Simultaneous Multiplexed Imaging of mRNA and Proteins with Subcellular Resolution in Breast Cancer Tissue Samples by Mass Cytometry. *Cell Systems* **6**, 25-36.e25 (2018).

Supplementary Information

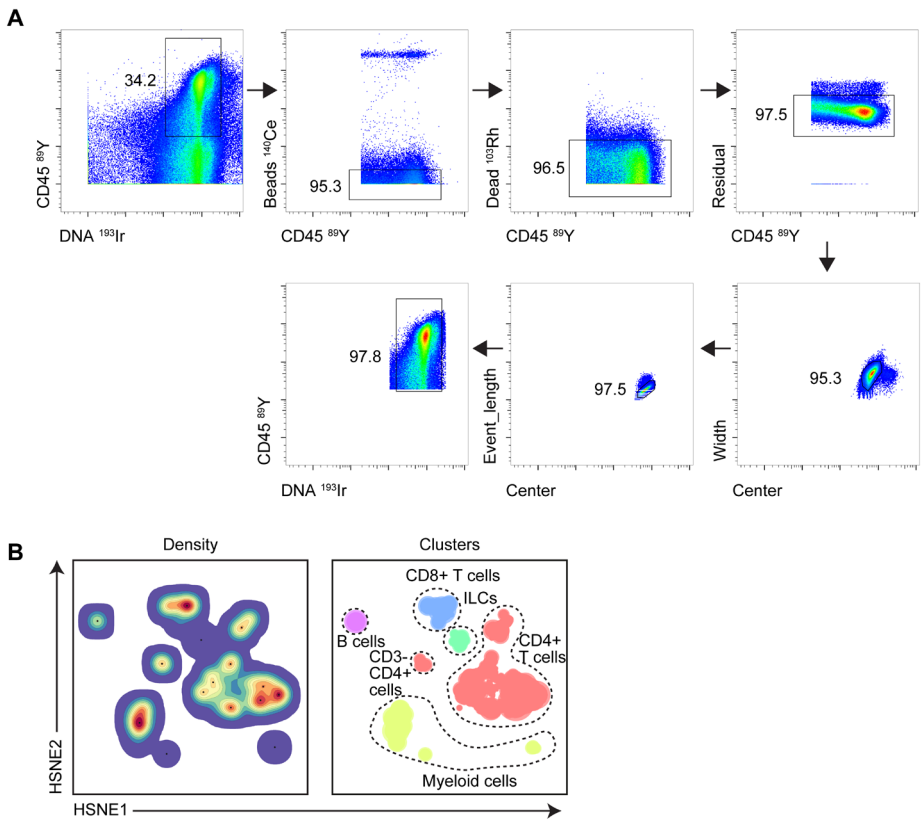

Figure S1 Gating strategy for single, live CD45⁺ cells on MF samples (A), and identification of the overview level of CD45⁺ cells by HSNE analysis (B).

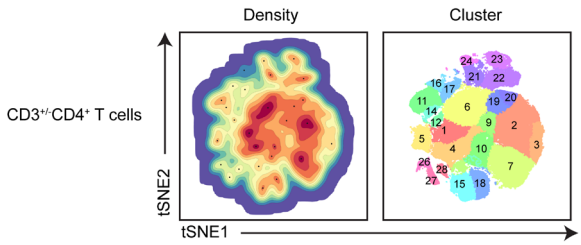

Figure S2 A collective t-SNE was performed on CD3⁻CD4⁺ T cells, and show the density map showing the local probability density of the embedded cells (left); Colors represent cluster partitions for per CD4⁺ T cells subpopulation (right).

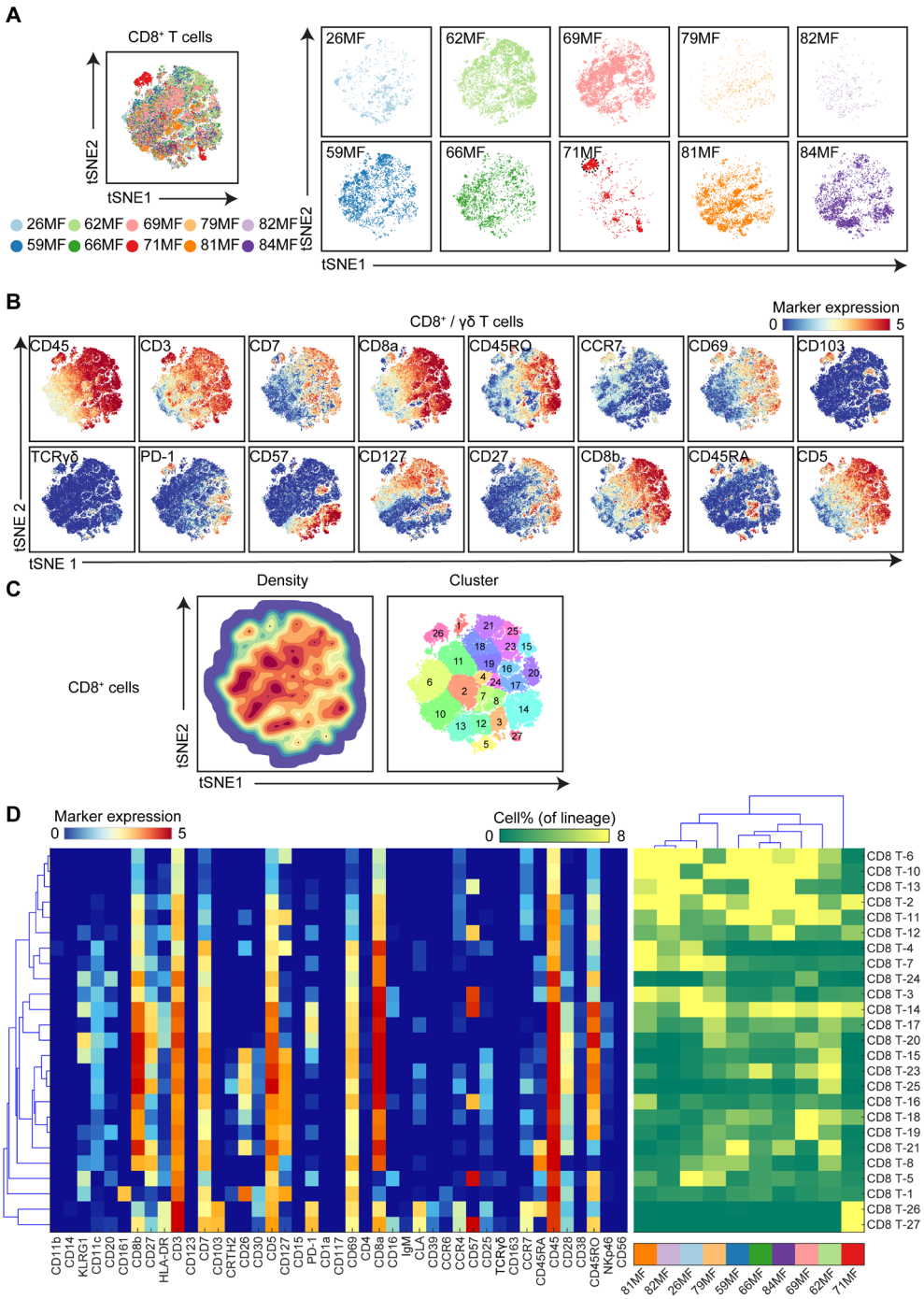

(Figure legend in next page)

Figure S3 Identification of phenotypically distinct clusters in the CD3⁺CD8⁺ T cell compartment across MF samples. (A) A collective t-SNE was performed on CD8⁺ T cells and stratified for samples (n = 10). In total, 5.1×104 CD8⁺ T cells were analyzed in the plots. **(B)** Relative expression level of indicated immune markers. Colors represent different level of marker expression. **(C)** The density map showing the local probability density of the embedded cells (left); Colors represent cluster partitions for per CD8⁺ T cells subpopulation (right). **(D)** Heatmap (blue-to-red scale) showing the median of marker expression values for the identified clusters and hierarchical clustering thereof; heatmap (green-to-yellow scale) showing the corresponding cell frequencies of identified clusters of total CD8⁺ T cells in each sample. The dendrogram shows the hierarchical clustering of samples. Colors represent different samples.

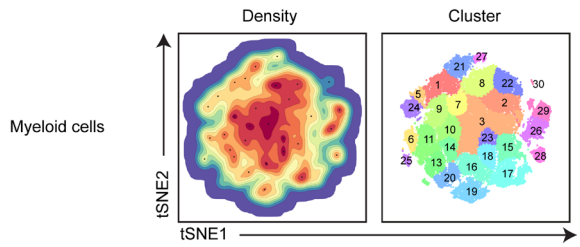

Figure S4 A collective t-SNE was performed on myeloid cells. The density map showing the local probability density of the embedded cells (left); Colors represent cluster partitions for per myeloid cells subpopulation (right).

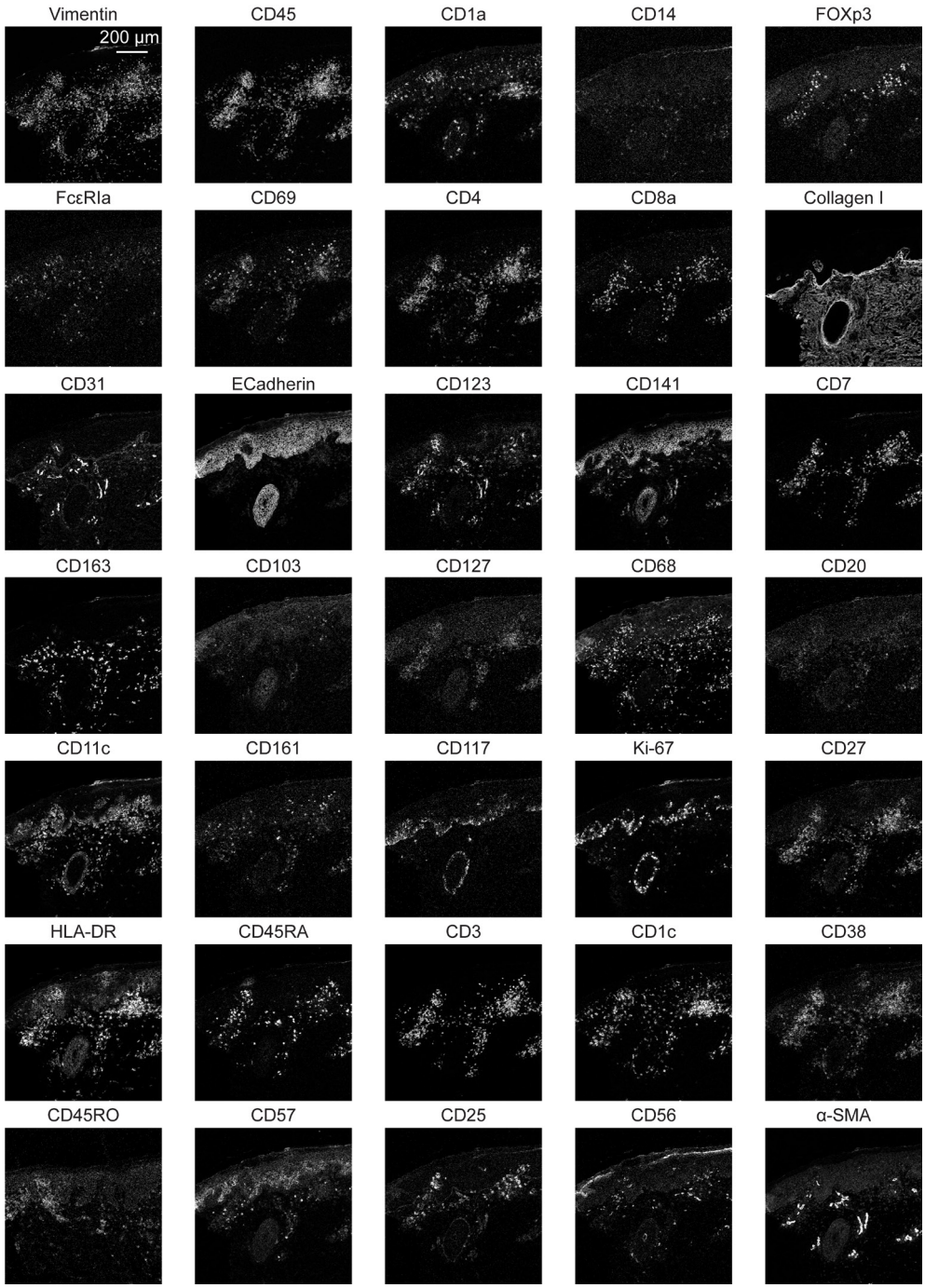

Figure S5 Individual antibody stains for representative MF patients (120MF) by IMC.

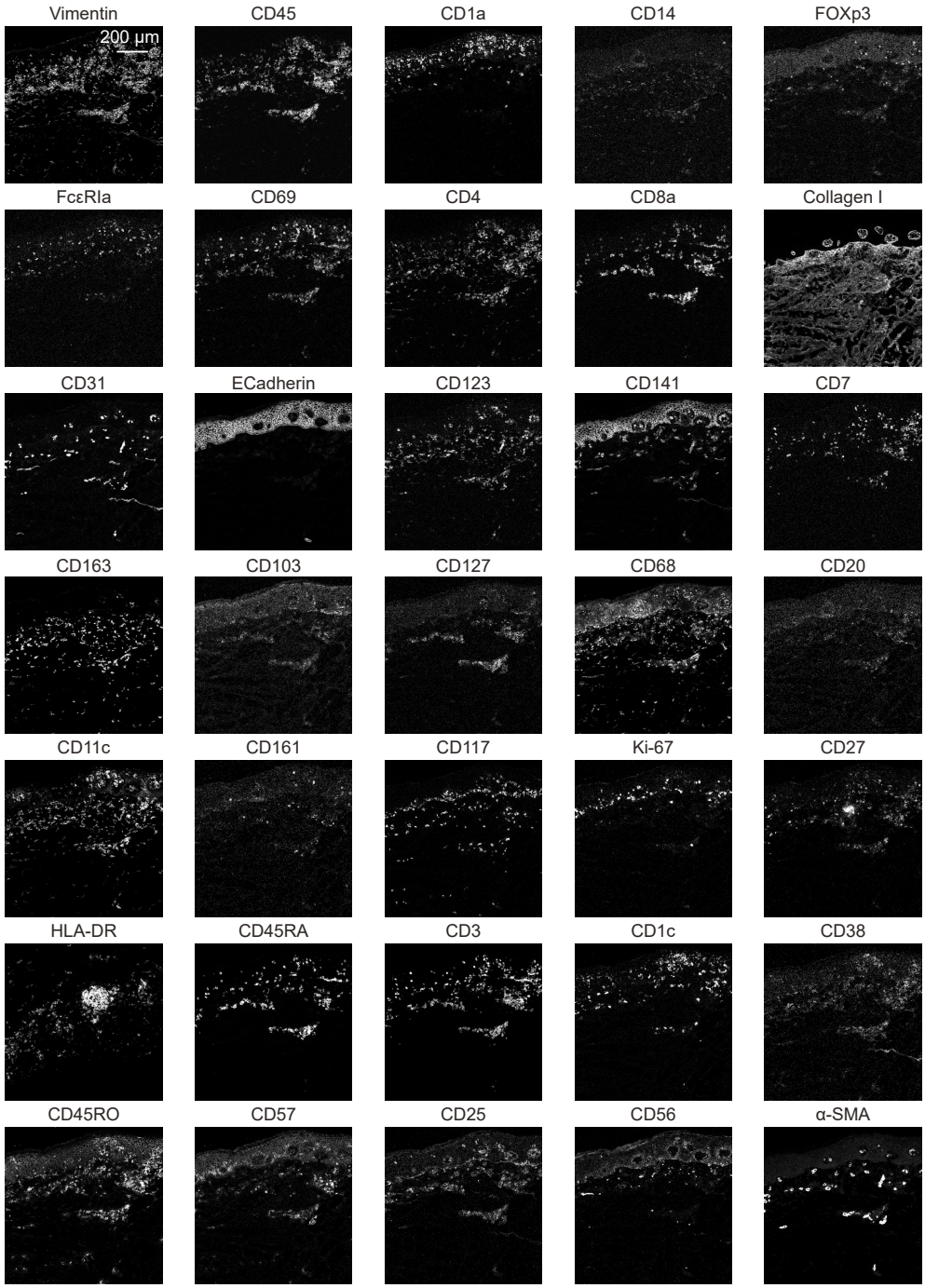

Figure S6 Individual antibody stains for 87MF patients by IMC.

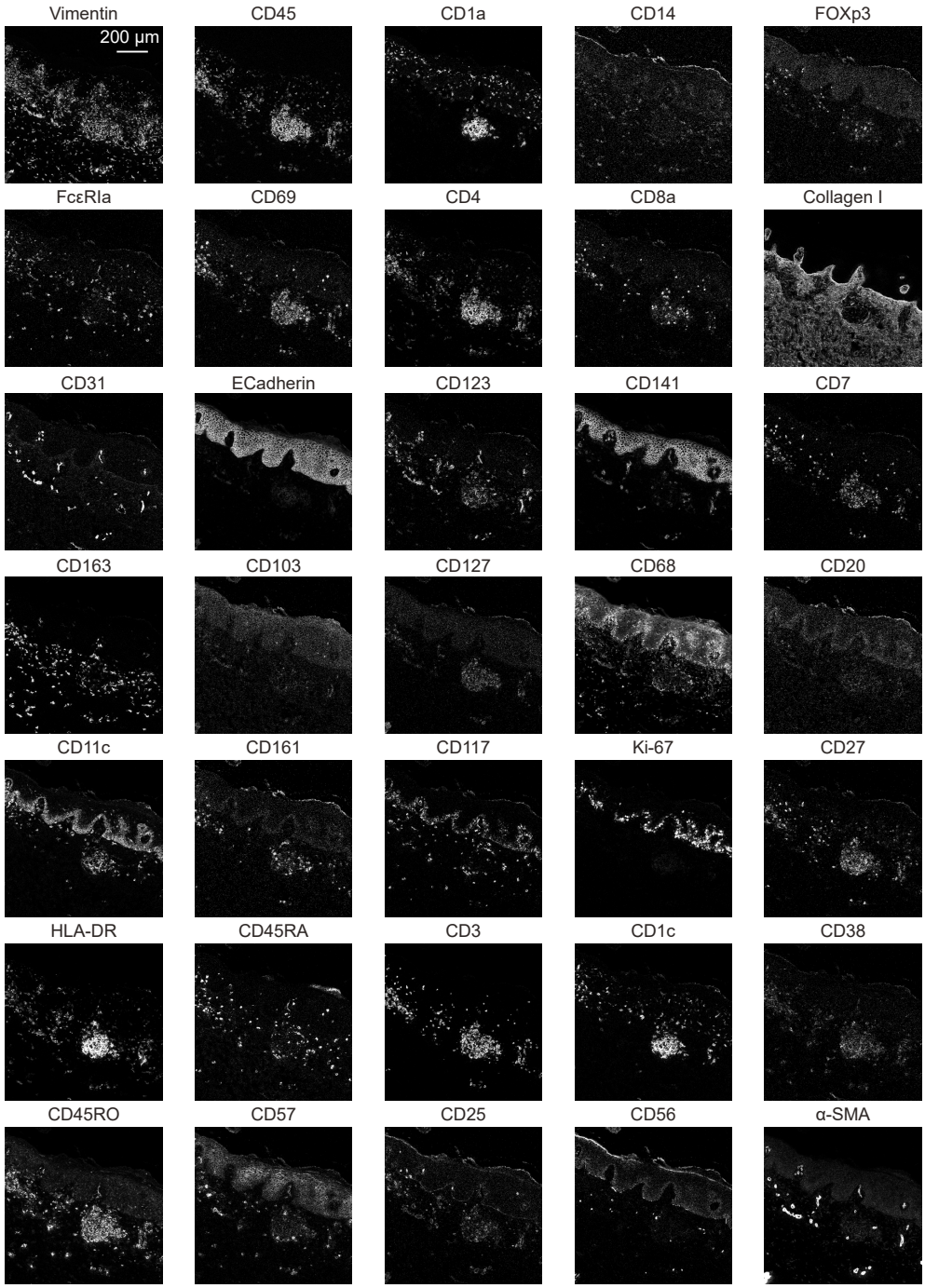

Figure S7 Individual antibody stains for 105MF patients by IMC.

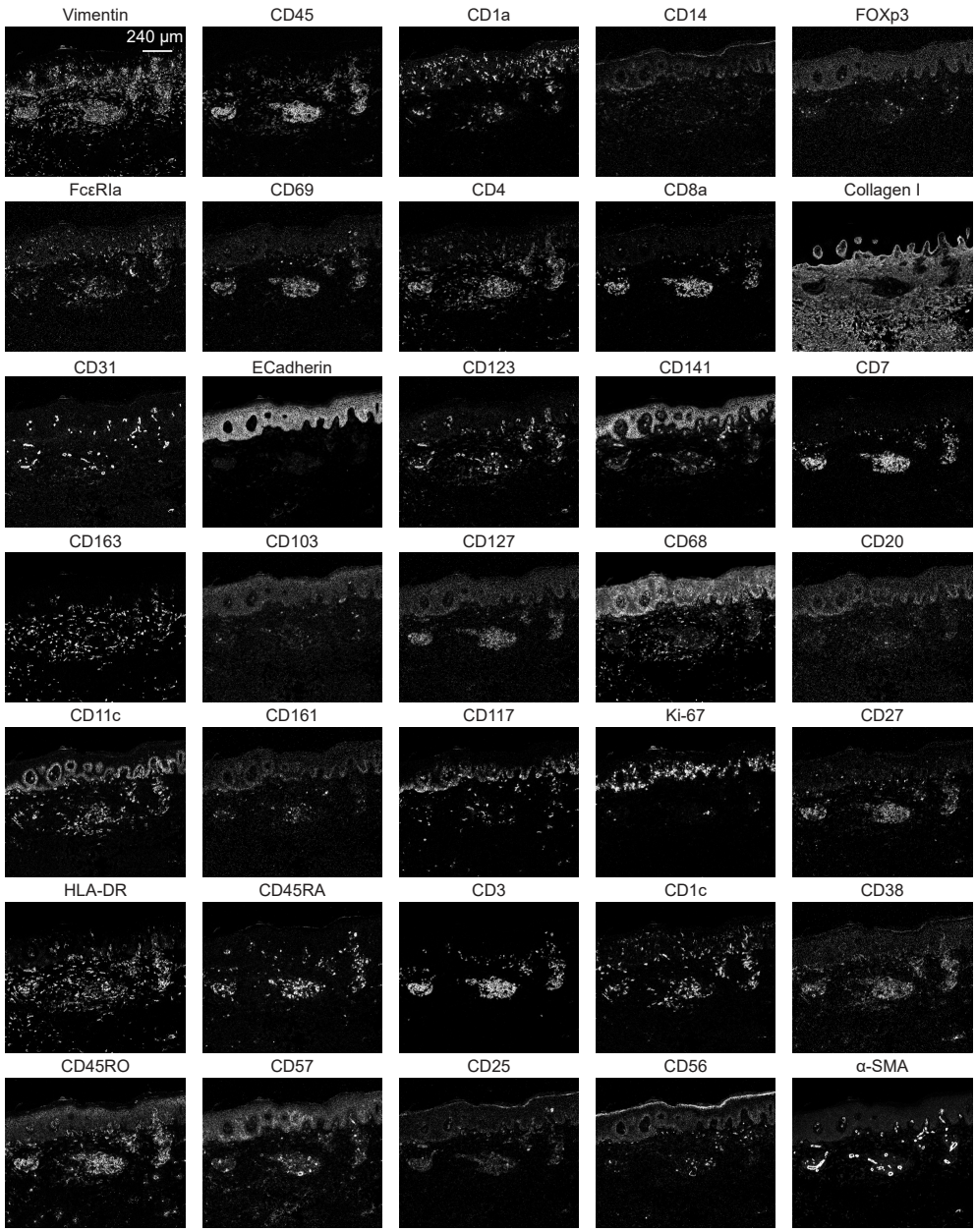

Figure S8 Individual antibody stains for 108MF patients by IMC.

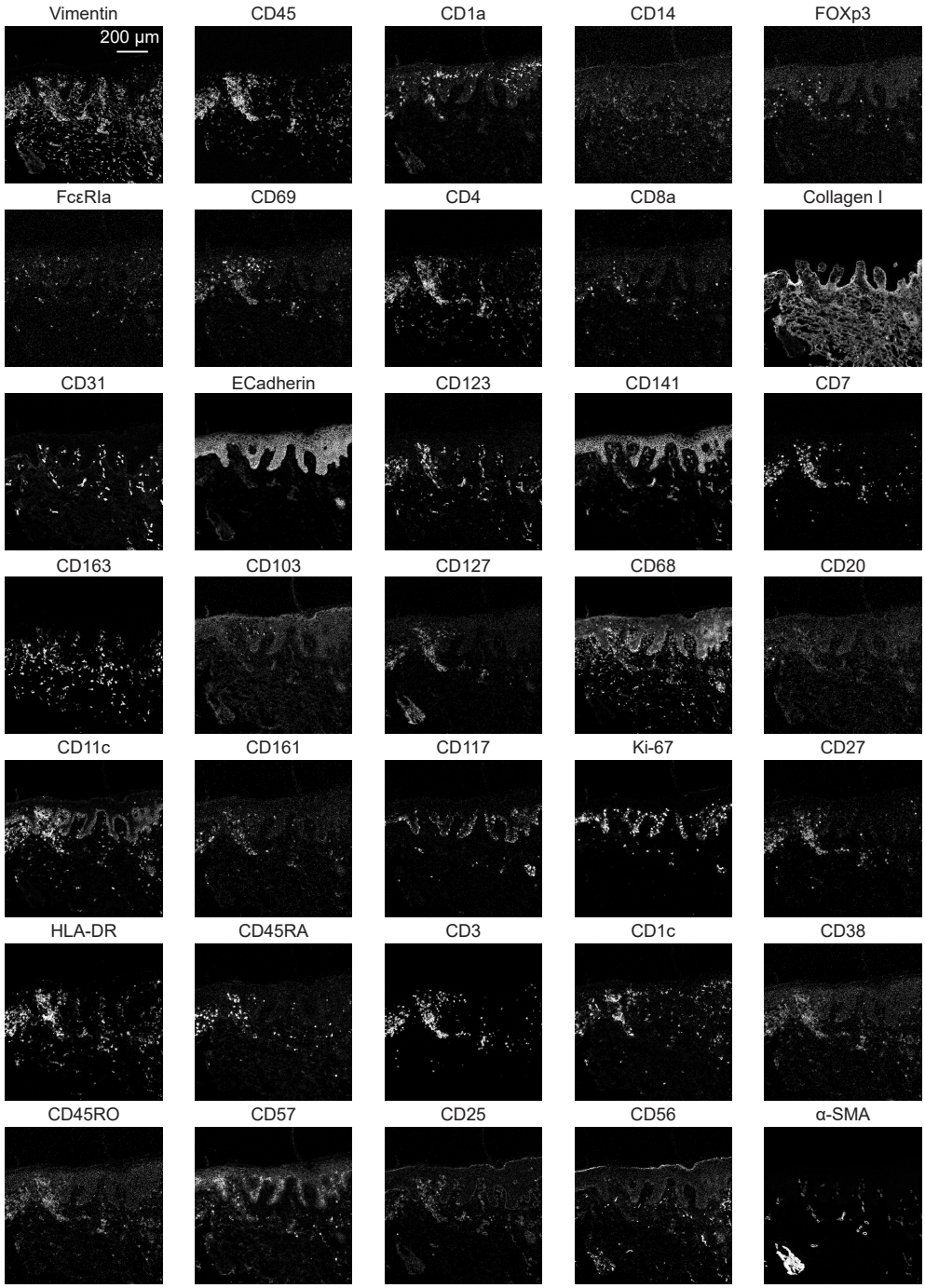

Figure S9 Individual antibody stains for 109MF patients by IMC.

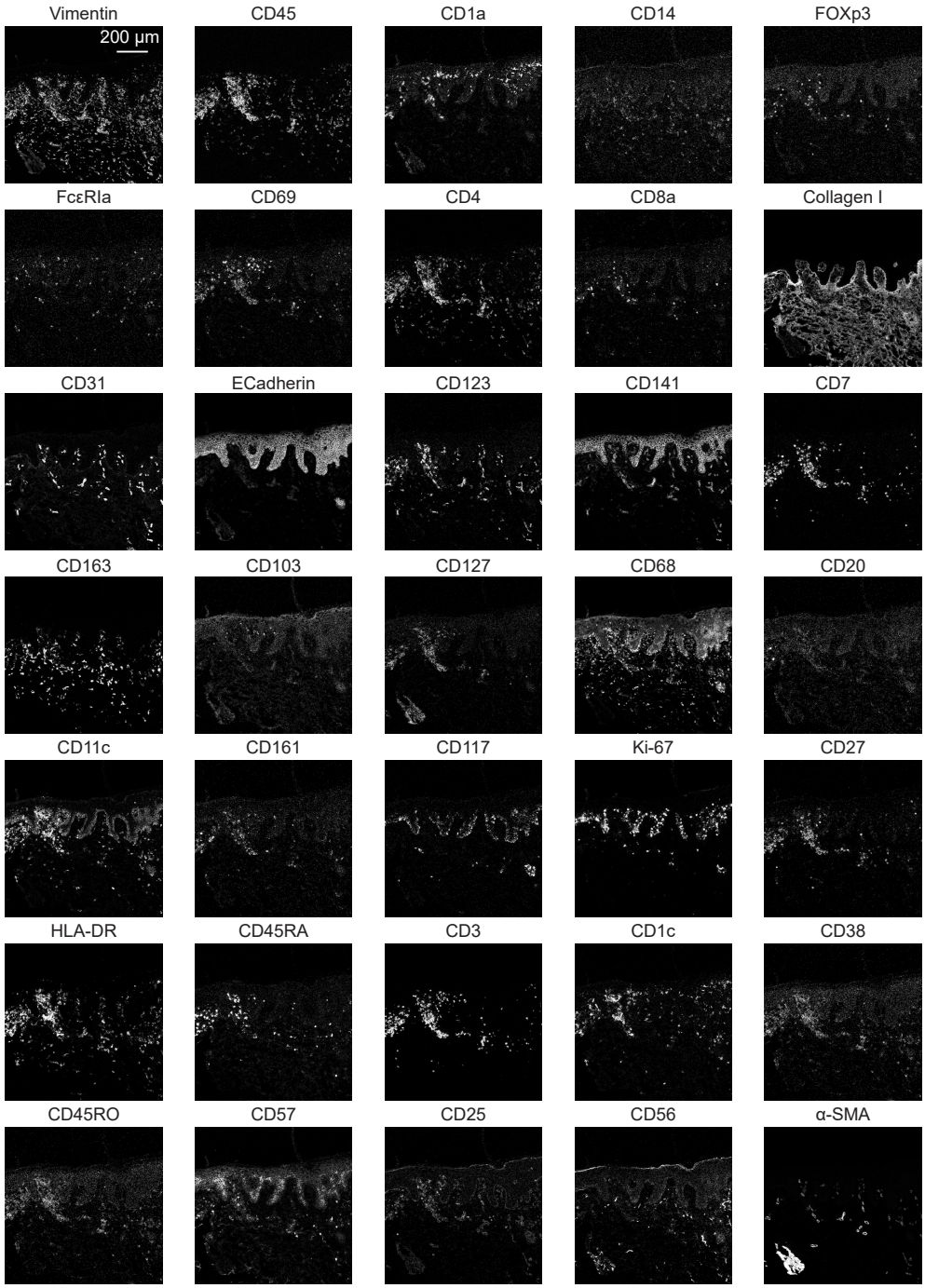

Figure S10 Individual antibody stains for 109MF patients by IMC.

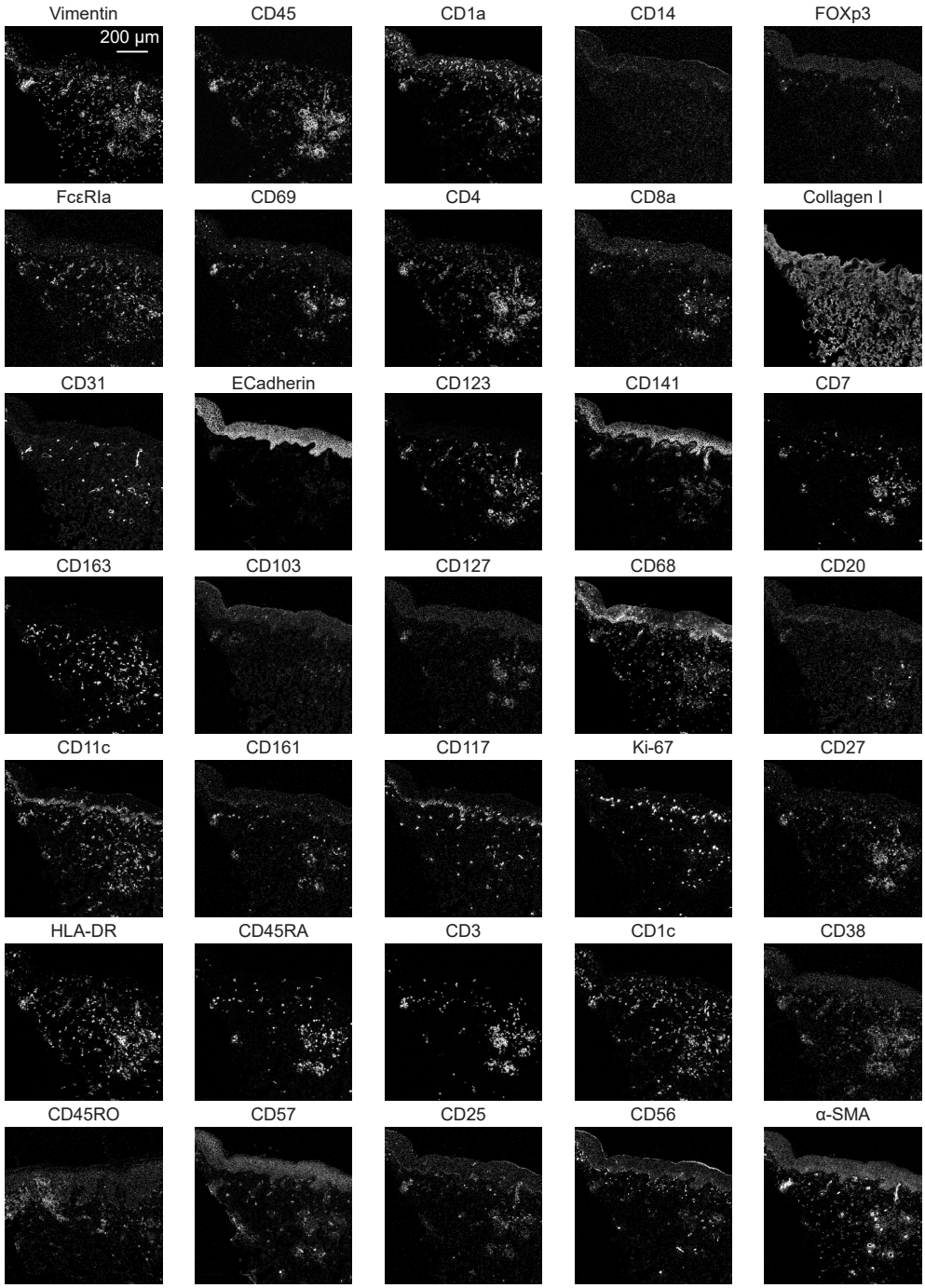

Figure S11 Individual antibody stains for 113MF patients by IMC.

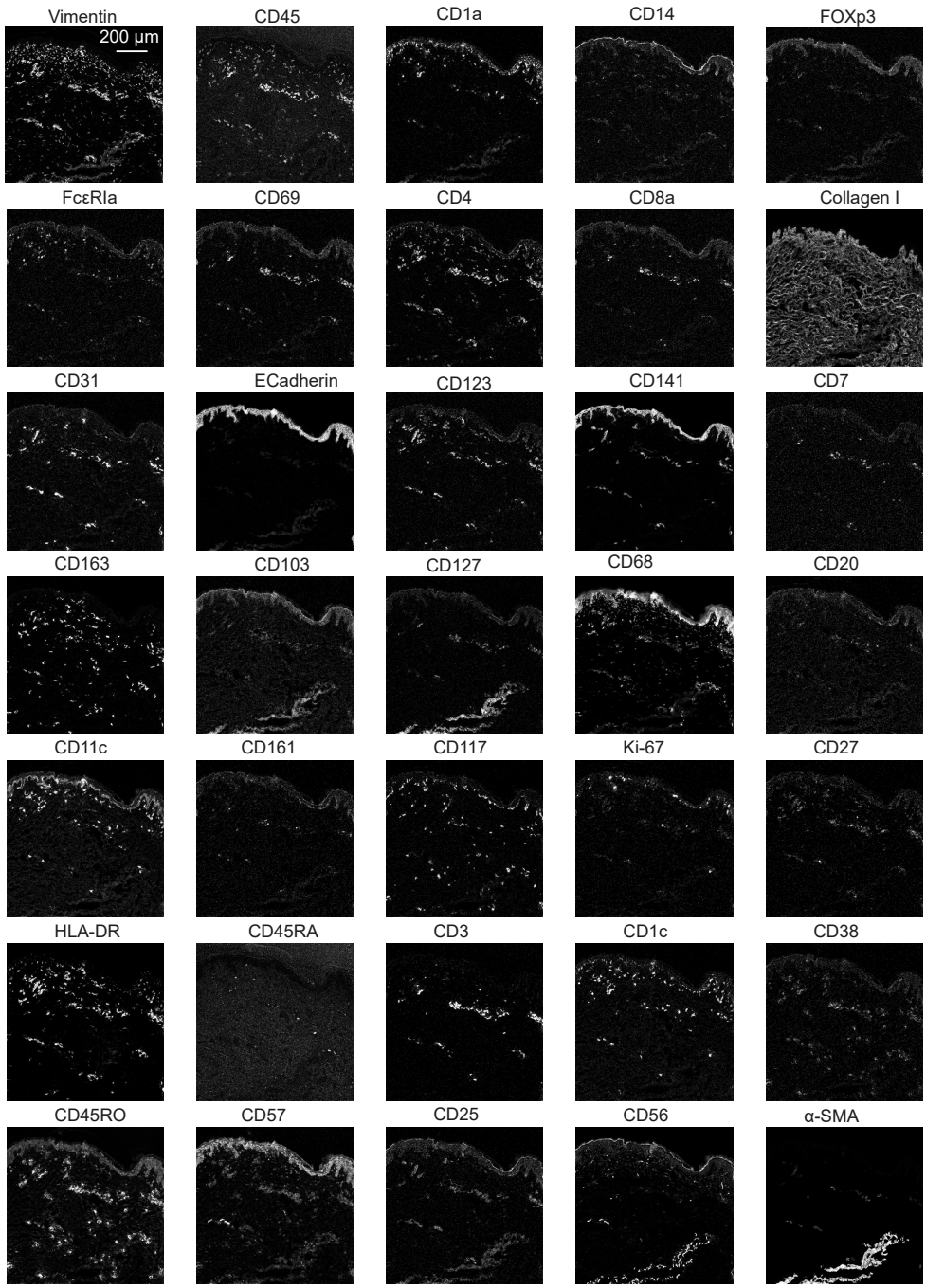

Figure S12 Individual antibody stains for 01NS patients by IMC.

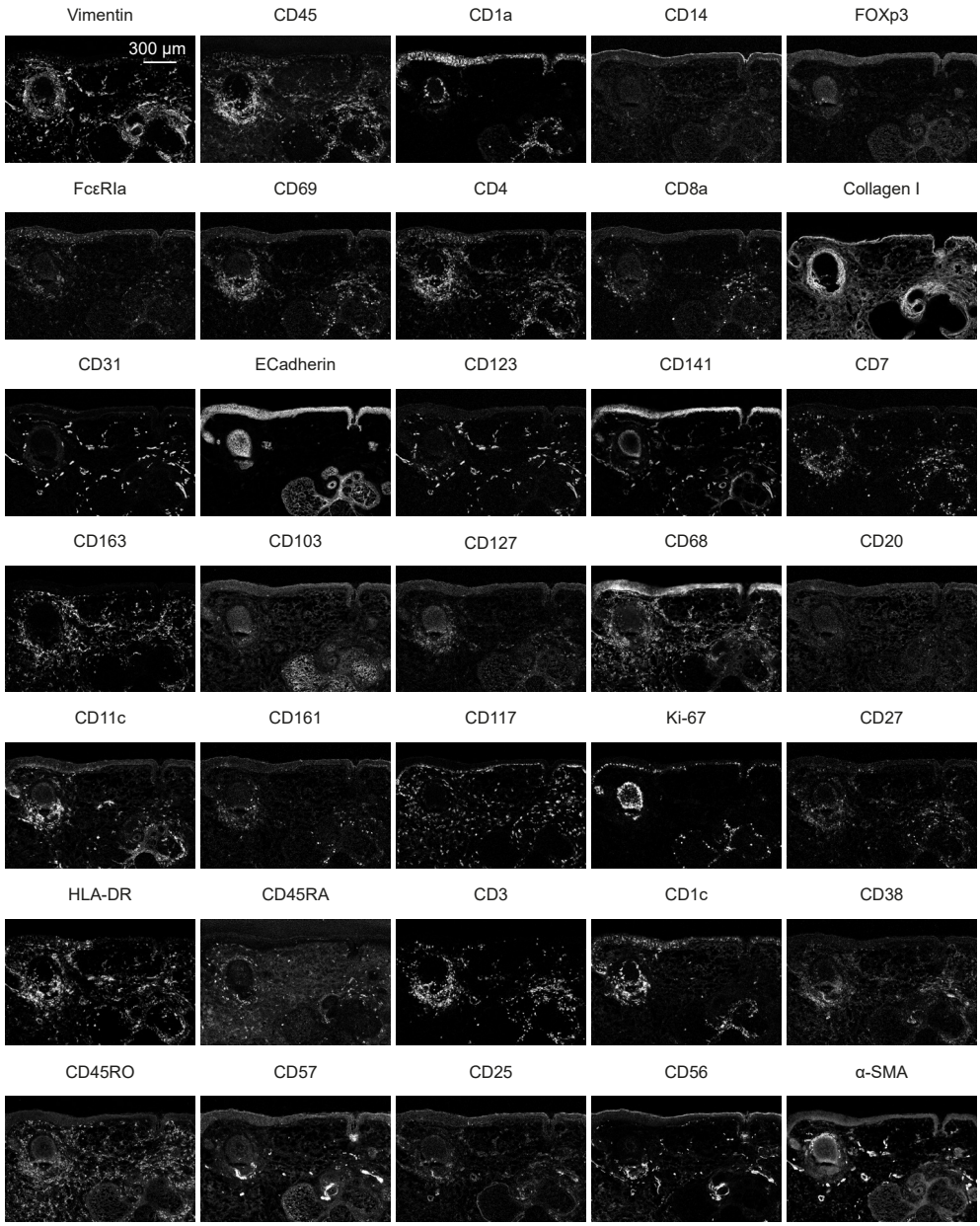

Figure S13 Individual antibody stains for 02NS patients by IMC.

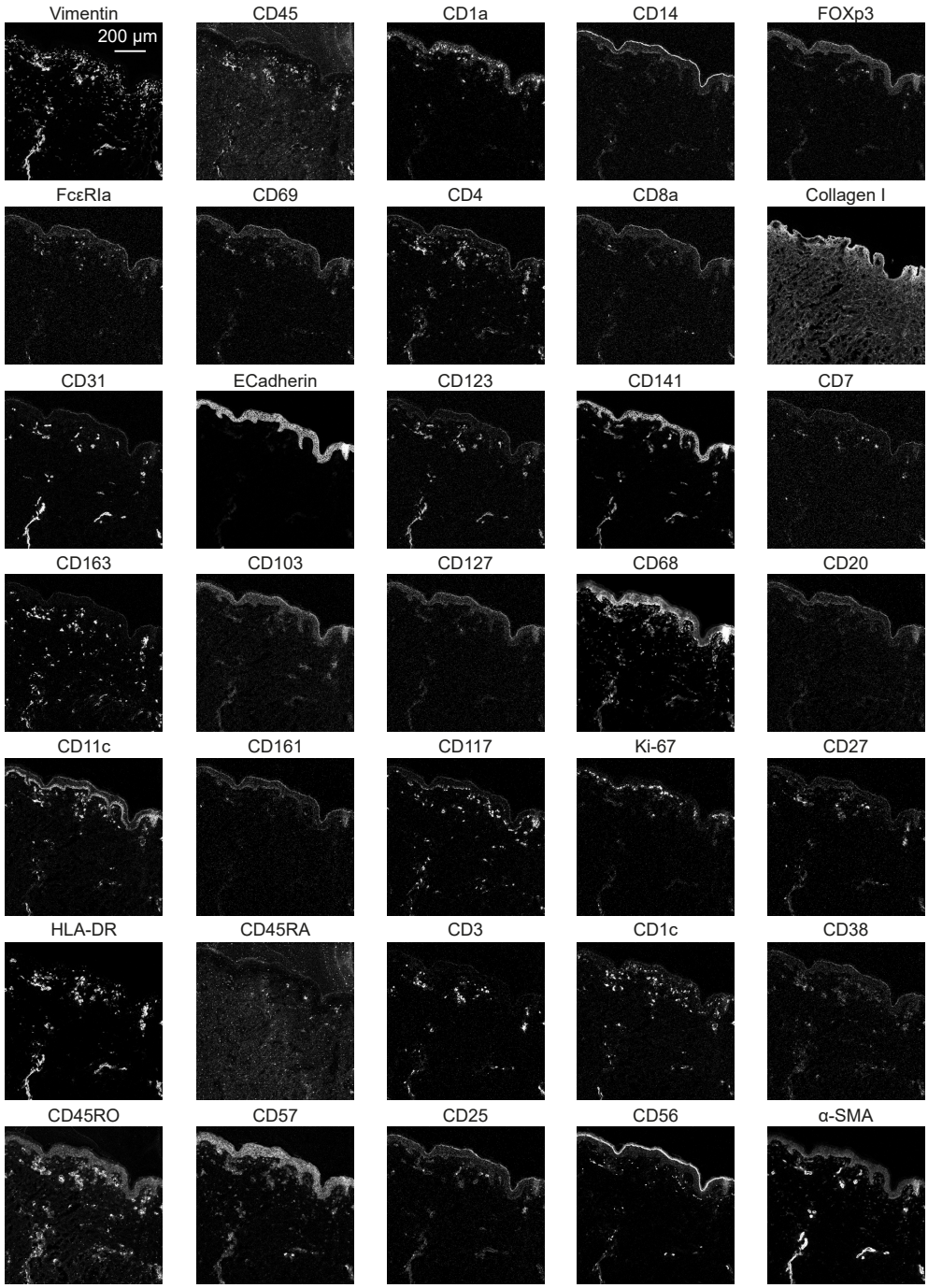

Figure S14 Individual antibody stains for 03NS patients by IMC.

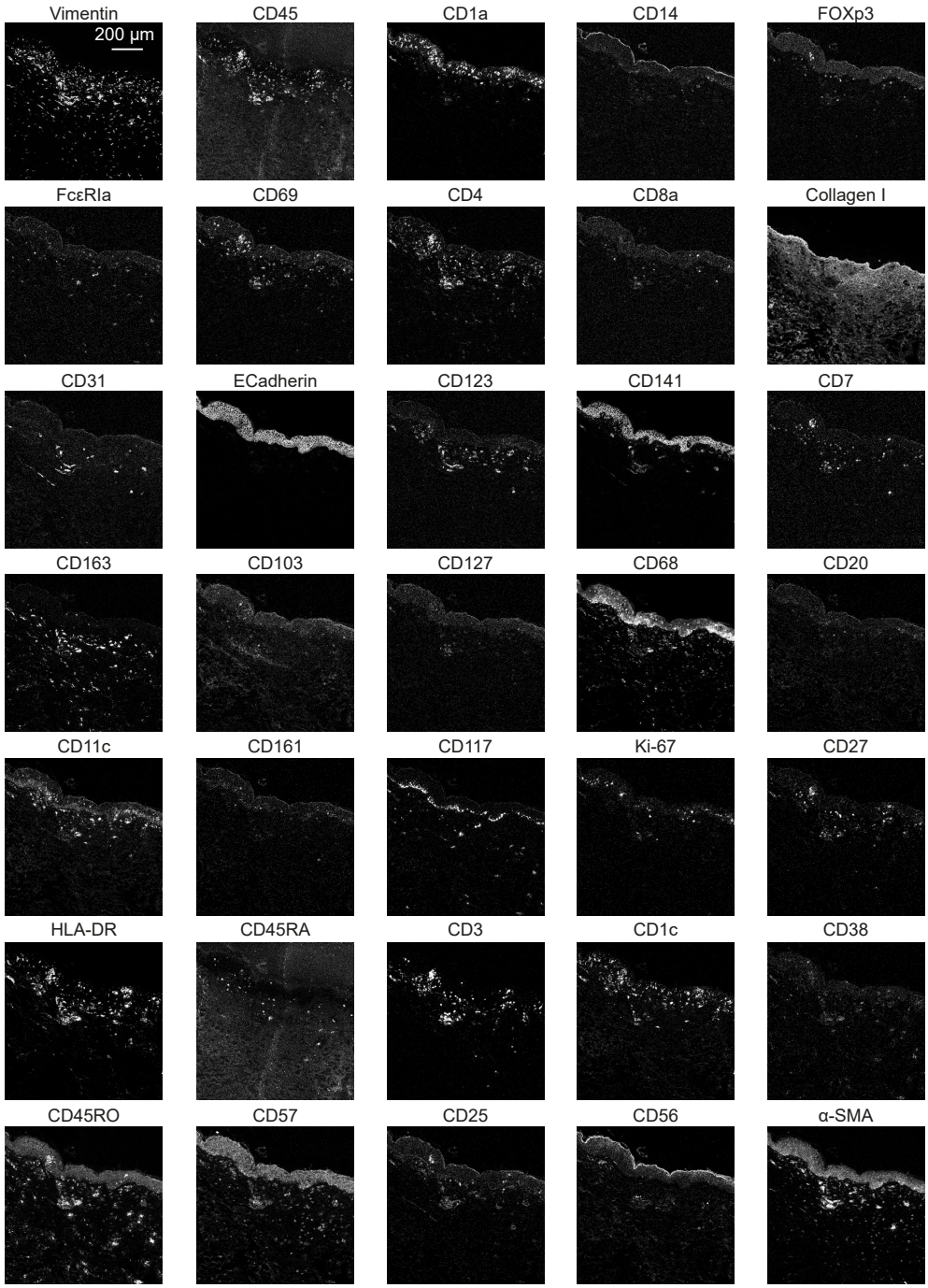

Figure S15 Individual antibody stains for 05NS patients by IMC.

Tables

Table S1 Characteristics of patients with Mycosis fungoides diseases.

Characteristics	MF patients by CyTOF (n=10)	MF Patients by IMC (n=6)
Sex (male:female)	6:4	4:2
Years of MF prior to biopsy		
Median	2	4
Range	0-21	2-8
Age at biopsy, years		
Median	54.5	62.5
Range	34-76	41-76
Stage at biopsy		
IA	0	1
IB	10	4
IIB	-	1
Follow-up, months		
Median	15	12
Range	12-20	8-20
Therapy after biopsy		
Topical corticosteroids	10	6
UV-therapy	5	-
Retinoids	2	-
Interferon-alpha	1	-
Radiotherapy	1	1
Disease course		
Progressive Disease	1	0
Stable disease	5	5
Partial Remission	2	1
Unknown	1	-

Table S2 The sex and age characteristics of the NS healthy donors.

Heathy Donors	IMC/CyTOF	Sex	Age
NS01	IMC	Female	78
NS02	IMC	Male	76
NS03	IMC	Male	41
NS04	IMC	Male	77
NS05	CyTOF	Male	62
NS06	CyTOF	Male	34
NS07	CyTOF	Male	78
NS08	CyTOF	Female	68
NS09	CyTOF	Male	52
NS10	CyTOF	Male	62
NS11	CyTOF	Female	73
NS12	CyTOF	Male	70
NS13	CyTOF	Male	70
NS14	CyTOF	Male	42
NS15	CyTOF	Male	70
NS16	CyTOF	Female	87
NS17	CyTOF	Male	74
NS18	CyTOF	Female	92
NS19	CyTOF	Male	86
NS20	CyTOF	Male	41
NS21	CyTOF	Male	81

Table S3 Single-cell suspension mass cytometry antibody panel.

	Antigen	Tag	Clone	Supplier	Cat.No	Dilution
1	CLA	104Pd	HECA-452	Biolegend	321302	1/50
2	CD39	108Pd	A1	Biolegend	328221	1/50
3	CD15	115In	W6D3	Biolegend	323035	1/50
4	CCR6	141Pr	G034E3	Fluidigm	31411003A	1/100
5	CD1a	142Nd	HI149	Sony	21100510	1/50
6	CD117	143Nd	104D2	Fluidigm	3143001B	1/100
7	CD69	144Nd	FN50	Fluidigm	3144018B	1/100
8	CD4	145Nd	RPA-T4	Fluidigm	3145001B	1/100
9	CD8a	146Nd	RPA-T8	Fluidigm	3146001B	1/200
10	CD57	147Sm	HNK-1	Biolegend	359602	1/200
11	CD16	148Nd	3G8	Fluidigm	3148004B	1/100
12	CD25	149Sm	2A3	Fluidigm	3149010B	1/100
13	IgM	150Nd	MHM88	Biolegend	314527	1/100
14	CD123	151Eu	6H6	Fluidigm	31511001B	1/100
15	TCRγδ	152Sm	11F2	Fluidigm	31512008B	1/50
16	CD7	153Eu	CD7-6B7	Fluidigm	3153014B	1/100
17	CD163	154Sm	GHI/61	Fluidigm	3154007B	1/100
18	CD103	155Gd	Ber-ACT8	Biolegend	350202	1/100
19	CRTH2	156Gd	BM16	Biolegend	350102	1/100
20	CD26	157Gd	BA5b	Biolegend	302702	1/100
21	CD30	158Gd	Ber-H2	Dako	M075101-2	1/50
22	CCR7	159Tb	G043H7	Fluidigm	3159003A	1/100
23	CD5	160Gd	UCHT2	Biolegend	300627	1/50
24	KLRG-1	161Dy	REA261	MACS	120-014-229	1/50
25	CD11c	162Dy	Bu15	Fluidigm	31612005B	1/200
26	CD20	163Dy	2H7	Biolegend	302343	1/200
27	CD161	164Dy	HP-3G10	Fluidigm	3164009B	1/100
28	CD127	165Ho	AO19D5	Fluidigm	3165008B	1/200
29	CD8b	166Er	SIDI8BEE	Ebio	15257407	1/50
30	CD27	167Er	O323	Fluidigm	3167002B	1/100
31	HLA-DR	168Er	L243	Biolegend	307651	1/300
32	CD45RA	169Tm	HI100	Fluidigm	3169008B	1/100
33	CD3	170Er	UCHT1	Fluidigm	3170001B	1/100
34	CD28	171Yb	CD28.2	Biolegend	302937	1/100
35	CD38	172Yb	HIT2	Fluidigm	31712007B	1/200
36	CD45RO	173Yb	UCHL1	Biolegend	304239	1/100
37	NKp46	174Yb	9E2	Biolegend	331902	1/40
38	PD-1	175Lu	EH 12.2H7	Fluidigm	3175008B	1/100
39	CD56	176Yb	NCAM16.2	Fluidigm	3176008B	1/100
40	CCR4	198Pt	205410	R & D	MAB1567-100	1/100
41	CD11b	209Bi	ICRF44	Fluidigm	3209003B	1/100
42	CD45	89Y	HI30	Fluidigm	3089003B	1/100
43	CD14	Qdot800	TüK4	ThermoFisher	Q10064	1/1000

Table S4 Imaging mass cytometry antibody panel on frozen skin tissue.

	Antigen	Tag	Clone	Supplier	Cat.	Dilution
1	CD1a	115In	010	Dako	M357101-2	1/50
2	CD14	141Pr	M5E2	BioL	301801	1/50
3	FOXp3	142Nd	236A/E7	eBioscience™	14-4777-82	1/100
4	FcεRIα	143Nd	AER-37 (CRA-1)	BioL	334602	1/50
5	CD69	144Nd	FN50	FLM	3144018B	1/50
6	CD4	145Nd	RPA-T4	FLM	3145001B	1/50
7	CD8a	146Nd	RPA-T8	FLM	3146001B	1/50
8	Collagen I	147Sm	polyclonal	Millipore	AB758	1/100
9	CD31	149Sm	89C2	CST	CST3528BF	1/100
10	E-cadherin	150Nd	24E10	CST	CST3195BF	1/50
11	CD123	151Eu	6H6	FLM	3151001B	1/50
12	CD141	152Sm	Phx-01	BioL	902102	1/50
13	CD7	153Eu	CD7-6B7	FLM	3153014B	1/100
14	CD163	154Sm	GHI/61	FLM	3154007B	1/100
15	CD103	155Gd	EPR4166	Abcam	ab221210	1/50
16	CD127	156Gd	R34.34	Beckman	18LIQ494	1/50
17	CD68	159Tb	KP1	FLM	3159035D	1/200
18	CD20	161Dy	H1	FLM	3161029D	1/50
19	CD11c	162Dy	S-HCL-3	BioL	125602	1/50
20	CD11c	162Dy	Bu15	FLM	3162005B	1/50
21	CD161	164Dy	HP-3G10	FLM	3164009B	1/50
22	CD117	165Ho	104D2	BioL	313202	1/50
23	Ki-67	166Er	D3B5	CST	CST9129BF	1/200
24	CD27	167Er	O323	FLM	3167002B	1/50
25	HLA-DR	168Er	L243	BioL	307651	1/800
26	CD45RA	169Tm	HI100	FLM	3169008B	1/100
27	CD3	170Er	UCHT1	FLM	3170001B	1/100
28	CD1c	171Yb	L161	BioL	331501	1/50
29	CD38	172Yb	HIT2	FLM	3172007B	1/100
30	CD45RO	173Yb	UCHL1	BioL	304239	1/50
31	CD57	174Yb	HNK-1/Leu-7	Abcam	Ab212403	1/100
32	CD25	175Lu	24204.0	Thermo	MA5-23714	1/50
33	CD56	176Yb	NCAM16.2	FLM	3176008B	1/50
34	αSMA	194Pt	1A4	CST	56856BF	1/100
35	Vimentin	198Pt	D21H3	CST	5741BF	1/100
36	CD45	89Y	HI30	FLM	3089003B	1/50
Fluidigm (Flui), Cell Signaling Technology (CST) and Biolegend (BioL)						

Table S5 The minimum and maximum threshold of each marker for per sample.

		NS01		NS02		NS03		NS04		87MF		105MF		106MF		109MF		113MF		120MF	
Channel	Marker	Min	Max	Min	Max	Min	Max	Min	Max	Min	Max	Min	Max	Min	Max	Min	Max	Min	Max	Min	Max
Y(89)	CD45	3	7.56	3	12.69	3	6.87	3	6.54	2	17.24	1	13.42	1	14.08	1	14.63	1	9.14	1	14.95
In(115)	CD1a	1	9.78	1	17.14	1	8.64	1	14.85	1	13.54	1	14.23	1	10.38	1	7.84	1	9.52	1	6.9
Pr(141)	CD14	1	4.22	1	4.13	1	5.2	1	3.5	1	3.23	0.5	3.8	1	3.51	1	3.34	1	2.83	1	3.03
Nd(142)	FOXP3	1	3.51	1	3.94	1	3.68	1	3.42	1	4.13	1	3.39	1	3.17	1	3.3	1	2.95	1.5	4.73
Nd(143)	FceRIα	1	3.64	1	3.52	1	3.17	1	3.06	1	4.64	1	5.73	1	4.61	1	3.48	1	5.2	1	3.59
Nd(144)	CD69	1	5.96	1	6.42	1	4.19	1	5.83	1	9.07	1	7.86	1	6.69	1	12.43	1	9	1	9.13
Nd(145)	CD4	1	8.12	1	9.3	1	6.28	1	6.87	1	8.82	1	11.11	1	8.22	1	10.87	1	7.79	1	7.61
Nd(146)	CD8a	1	5.12	1	4.98	1	3.33	1	3.1	1	10.82	1	10	1	10	1	10	1	8	1	10
Sm(147)	Collagen I	3	22.54	3	40.83	3	18.44	3	16.54	3	36.48	3	28.47	3	35.67	3	44.56	3	37.37	3	41.06
Sm(149)	CD31	3	23.58	3	29.34	3	22.96	1	5.42	3	27.81	3	17.62	3	23.52	3	34.06	3	14.84	3	23.49
Nd(150)	E-cadherin	3	44.14	3	55.93	3	37.57	3	32.67	3	27.2	3	28.28	3	30.02	3	28.08	3	26.68	3	24.93
Eu(151)	CD123	1	5.91	1.5	7.73	1	4.48	1	4.27	1	7.1	1	6.22	1	7.21	1	8.45	1	9.98	1	8.55
Sm(152)	CD141	1	22.26	3	27.95	3	17.13	3	16.54	3	15.22	3	21.35	3	17.98	3	19.68	2	15.44	3	13.94
Eu(153)	CD7	1	3.01	1	7.06	1	3.05	1	3.97	1	7.54	1	7.12	1	10.54	1	15.26	1	9.24	1	12.03
Sm(154)	CD163	3	30.43	1	20.83	1	16.89	2	15.73	2	54.73	3	32.38	3	36.23	2	41.86	1	20.47	1	23.33
Gd(155)	CD103	1	4.51	3	6.25	1	3.96	1	3.87	1	4.18	1	3.72	1	3.55	1	3.73	1	3.4	1	3.61
Gd(156)	CD127	1	6.4	1	4.11	1	3.29	0.5	3.13	1	4.58	1	3.84	1	3.8	1	4.75	1	3.51	1	3.68
Tb(159)	CD68	3	73.69	3	89.96	3	77.5	3	52.22	8	68.11	8	101.4	8	101.3	5	81.17	8	52.32	10	63.97
Dy(161)	CD20	1	3.44	2	3.63	1	3.4	1	3.14	1	3.47	1	3.34	1	3.16	1	3.2	1	3.64	1	3.23
Dy(162)	CD11c	3	9.55	3	13.65	3	8.46	3	7.06	3		3	14.13	3	12.33	3	14.89	2	13.34	3	16.88
Dy(164)	CD161	1	3.61	1	4.35	1	3.36	1	3.27	1	4.22	1	4.99	1	3.59	1	4.59	1	5.24	1	4.73
Ho(165)	CD117	1	13.62	1	13.62	1	11.85	1	15.73	1	15.46	1	10.99	1	13.61	1	9.14	1	9.16	1	6.33
Er(166)	Ki-67	1	8.35	1	19.62	1	13.21	1	5.79	1	13.6	1	25.18	1	21.68	1.5	25.96	1	15.77	1.5	16.44
Er(167)	CD27	1	4.55	0	5.45	1	6.43	1	7.31	1	10.76	1	7.14	1	6.5	1	7.57	1	6.67	1	6.73
Er(168)	HLA-DR	3	44.68	3	33.07	3	39.48	1	28.32	2	31.61	3	62.1	3	36.67	1	38.63	2	29.65	3	45.24
Tm(169)	CD45RA	3	8.84	3	8.64	3	9.55	3	7.76	3	70.32	2	21.36	2	20.26	3	21.42	2	25.68	2	25.35
Er(170)	CD3	1	25.74	1	20.68	1	16.74	1	17.71	1	29.95	1	20.8	1	25.46	1	27.53	1	18.94	1	22.41
Yb(171)	CD1c	1	10.98	1	10.54	1	9.62	1	9.47	1	13.22	1	17.29	1	12.87	1	9.8	1	13.53	1	16.51
Yb(172)	CD38	1	3.8	1	4.94	1	3.64	0.6	3.41	1	4.03	1	3.92	1	4.07	1	3.74	1	3.74	1	5.15
Yb(173)	CD45RO	3	28.42	3	51.66	3	21.86	3	20.36	3	26.56	3	26.05	3	23.51	3	27.58	3	23.54	3	26.98
Yb(174)	CD57	3	18.04	3	26.96	3	16.73	3	13.9	3	7.48	3	7.03	3	6.03	3	8.22	2	5.29	3	7.41
Lu(175)	CD25	1	4.17	1	4.35	1	4.32	1	4.24	1	5.21	1	4.32	1	3.97	1	3.99	0.5	3.67	1	6.28
Yb(176)	CD56	3	43.53	3	24.62	3	18.92	1	7.57	3	8.92	3	9.86	3	7.72	3	21.11	3	17.75	2	9.28
Pt(194)	αSMA	10	463.4	10	26.8	10	50.12	10	10.75	10	76.44	10	41.03	10	45.27	10	192.7	5	11.89	10	35.51
Pt(198)	Vimentin	5	129.4	5	175.8	5	117.4	5	95.46	5	175.5	5	113.5	5	117.7	5	116.3	3	116.5	5	117.8